AI-based classification of anticancer drugs reveals nucleolar condensation as a predictor of immunogenicity

Giulia Cerrato, Peng Liu, Liwei Zhao, Adriana Petrazzuolo, Juliette Humeau, Sophie Theresa Schmid, Mahmoud Abdellatif, Allan Sauvat, Guido Kroemer

Cerrato *et al. Molecular Cancer* (2024) 23:275
https://doi.org/10.1186/s12943-024-02189-3

Molecular Cancer

RESEARCH Open Access

AI-based classification of anticancer drugs reveals nucleolar condensation as a predictor of immunogenicity

Giulia Cerrato[1,2,3*], Peng Liu[1,2,3], Liwei Zhao[1,2,3], Adriana Petrazzuolo[1,3,4], Juliette Humeau[1,3,5], Sophie Theresa Schmid[6,7], Mahmoud Abdellatif[1,3,6,7], Allan Sauvat[1,2,3*†] and Guido Kroemer[1,2,3,8,9*†]

Abstract

Background Immunogenic cell death (ICD) inducers are often identified in phenotypic screening campaigns by the release or surface exposure of various danger-associated molecular patterns (DAMPs) from malignant cells. This study aimed to streamline the identification of ICD inducers by leveraging cellular morphological correlates of ICD, specifically the condensation of nucleoli (CON).

Methods We applied artificial intelligence (AI)-based imaging analyses to Cell Paint-stained cells exposed to drug libraries, identifying CON as a marker for ICD. CON was characterized using SYTO 14 fluorescent staining and holotomographic microscopy, and visualized by AI-deconvoluted transmitted light microscopy. A neural network-based quantitative structure-activity relationship (QSAR) model was trained to link molecular descriptors of compounds to the CON phenotype, and the classifier was validated using an independent dataset from the NCI-curated mechanistic collection of anticancer agents.

Results CON strongly correlated with the inhibition of DNA-to-RNA transcription. Cytotoxic drugs that inhibit RNA synthesis without causing DNA damage were as effective as conventional cytotoxicants in inducing ICD, as demonstrated by DAMPs release/exposure and vaccination efficacy in mice. The QSAR classifier successfully predicted drugs with a high likelihood of inducing CON.

Conclusions We developed AI-based algorithms for predicting CON-inducing drugs based on molecular descriptors and their validation using automated micrographs analysis, offering a new approach for screening ICD inducers with minimized adverse effects in cancer therapy.

Keywords Artificial intelligence, Automated image analysis, Neural network, Cancer chemotherapy, Immunogenic cell death, Integrated stress response, Transcription inhibition

†Allan Sauvat and Guido Kroemer contributed equally to this work.

*Correspondence:
Giulia Cerrato
giulia.cerrato@gustaveroussy.fr
Allan Sauvat
allan.sauvat@gustaveroussy.fr
Guido Kroemer
kroemer@orange.fr

Full list of author information is available at the end of the article

Background

Immunogenic cell death (ICD) affecting highly antigenic malignant cells constitutes a desirable outcome of therapeutic interventions that lead to the (re)activation of cancer immunosurveillance [1–4] and enhance sensitivity to immunotherapy with immune checkpoint inhibitors targeting CTLA-4 or the PD-1/PD-L1 interaction, as initially demonstrated by preclinical experimentation [5]. Clinical trials have confirmed that so-called induction therapies, including chemotherapy with ICD-inducing cytotoxicants, can be favorably combined with subsequent immunotherapy. This has been exemplified for colon cancer [6], esophageal and gastric junctional carcinoma [7–9], as well as for triple-negative breast cancer [10–12]. ICD is not linked to a particular cell death subroutine (such as apoptosis, ferroptosis, necroptosis and pyroptosis) [1–4], consistent with observations that anticancer drugs often stimulate a mixture of different cell death types [13]. Rather, ICD requires a particular pattern of premortem stress responses that lead to the release of danger-associated molecular patterns (DAMPs) such as adenosine triphosphate (ATP), the secretion of Type-1 interferons (IFNs), as well as to the exposure of the normally endoplasmic reticulum (ER)-sessile protein calreticulin (CALR) at the surface of cells. ATP chemoattracts myeloid cells into the tumor bed, and surface CALR renders them palatable to dendritic cells, allowing for the engulfment of portions of malignant cells and the presentation of tumor-associated antigens to cytotoxic T lymphocytes, which are recruited as a result of the Type-1 interferon response [14–16]. Additional ICD-relevant DAMPs such as annexin A1 and high-mobility group B1 (HMGB1), which are released postmortem, also contribute to the stimulation of immunocytes invading the tumor [17, 18].

Notably, not all chemotherapeutics are equal in their capacity to stimulate ICD. A minority of cytotoxicants are highly effective in eliciting ICD, while most kill neoplastic cells without igniting a therapeutically relevant immune response [1, 19]. For this reason, phenotypic screens were developed to discriminate ICD inducers from non-ICD inducers and to identify novel ICD inducers in compound libraries. Thus, biosensor cells that allow the measurement of ATP release, CALR exposure, HMGB1 release and Type-1 interferon responses were generated and used in screening campaigns [20, 21] to successfully identify novel ICD inducers that were FDA approved (such as lurbinectidin for the treatment of small cell lung cancer and belantamab mafodotin for multiple myeloma) or are currently undergoing Phase-II evaluation [22–25].

Research in cell biology led to the discovery that some aspects of the ER stress response such as the phosphorylation of eukaryotic initiation factor 2a (eIF2α) by a specific set of kinases was required for premortem ATP release as well as for CALR exposure [26]. Indeed, eIF2α phosphorylation is considered as pathognomonic for ICD [27], and this notion is supported by studies performed on patient-derived tumors [28]. Inhibition of DNA-to-RNA transcription is another salient feature of ICD that likely occurs upstream of eIF2α phosphorylation, as it starts already to take place half an hour after treatment [29]. Thus, quantitative measurements of eIF2α phosphorylation and RNA synthesis can be incorporated into phenotypic screens for the discovery of ICD inducers [27, 30]. However, screens that measure multiple parameters (release of ATP, HMGB1 and Type 1 interferons, CALR exposure, eIF2α phosphorylation and transcriptional inhibition) are both expensive and impractical.

The present study was designed to identify ICD-associated phenotypic changes occurring in cancer cells using artificial intelligence (AI). Neural network-aided image analyses revealed nucleolar condensation (CON) as a feature that strongly correlates with inhibition of RNA synthesis as well as with ICD. Of note, CON can be detected by brightfield imaging and hence does not require the use of fluorescent biosensors but solely transmitted light (TL). We observed that cytotoxic drugs that induce CON and suppress transcription potently induce ICD even in the absence of a DNA damage response. Moreover, we built an AI tool that identifies drugs inducing ICD based on their molecular structure.

Results

Automated analysis of cell painting images identifies altered nucleoli as a feature of transcriptional inhibition

Cell Painting is a high-content image-based technology for morphological profiling of cells stained with multiplexed fluorescent dyes that label different cellular structures such as DNA (Hoechst 33342), endoplasmic reticulum (concanavalin A/Alexa Fluor 488), F-actin cytoskeleton (phalloidin/Alexa Fluor 568), mitochondria (MitoTracker Deep Red) and RNA (SYTO 14 green fluorescent stain) [31]. To identify cell morphological changes that accompany the inhibition of transcription (the earliest ICD feature) in an hypothesis-agnostic fashion, human osteosarcoma U2OS cells, which are often used in ICD screens [20, 32], were exposed in multi-well cultures to a home-made library composed of chemotherapeutic agents and inhibitors of DNA-to-RNA transcription that includes several validated ICD inducers [1, 19–21, 30] and then subjected to Cell Painting (Fig. 1a). In the subsequent step, cell micrographs were acquired by automated confocal and brightfield microscopy (as displayed in Fig. 1b). After image segmentation and extraction of relevant primitives, cellular features from populations that were either left untreated or treated with transcription inhibitors, were used for training a

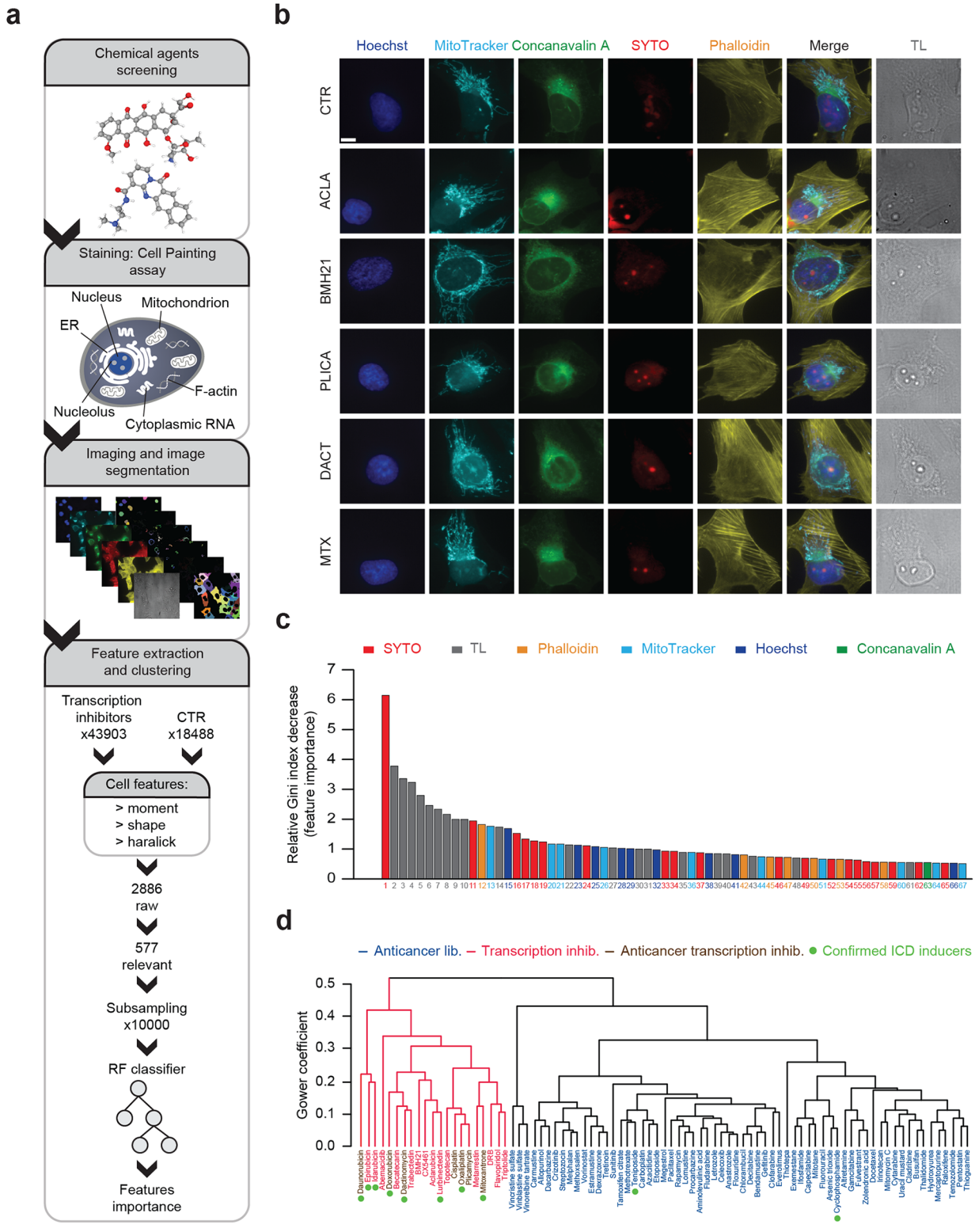

Fig. 1 (See legend on next page.)

(See figure on previous page.)

Fig. 1 Unbiased morphological profiling of anticancer agents using cell painting assay. (**a**) An overview of the strategy for the screening procedure is illustrated. Human osteosarcoma U2OS cells were treated with a custom-built anticancer library at 3 µM, while cisplatin was used at 300 µM and oxaliplatin at 500 µM, supplemented with a selection of agents inhibiting transcription (i.e. 3 µM epirubicin, 3 µM idarubicin, 10 µM abemaciclib, 1 µM becatecarin, 1 µM trabectedin, 5 µM BMH21, 1 µM CX5461, 15 µM aclarubicin, 1 µM lurbinectedin, 50 µM topotecan, 20 µM metarrestin, 200 µM DRB, 1 µM flavopiridol, 1 µM triptolide) or left untreated (CTR), for 4 h. Subcellular organelles were stained according to the cell painting assay and cells were subjected to high-content microscopy, image segmentation and subsequent cell features extraction. After sub-setting two groups from the dataset, i.e. transcription inhibitors and untreated (CTR) group, a random forest (RF) binary classifier was trained, and feature importances were thereafter extracted from the latter. (**b**) Representative fluorescence and transmitted light (TL)-based images show the panel of acquired channels, i.e. Hoechst 33342 (nucleus, DNA; DAPI channel), MitoTracker Deep Red (mitochondria; Cy5 channel), concanavalin A (endoplasmic reticulum; FITC channel), SYTO 14 (nucleoli, cytoplasmic RNA; Cy3 channel), phalloidin (actin; Texas Red channel) and TL (brightfield), for a selection of agents. Scale bar equals 10 µm. (**c**) The displayed relative Gini index decrease represents the importance of features for classification. Colors represent the acquisition channels from which the feature was extracted. (**d**) Hierarchical cluster dendrogram based on the weighted distance matrix calculated using Gower's similarity coefficient identifies a grouping pattern of the evaluated chemical compounds. Agents from the custom-built anticancer library are depicted in blue, supplemental transcription inhibitors in rose red, anticancer transcription inhibitors in brown and an adjacent green dot indicates confirmed immunogenic cell death (ICD) inducers

random forest (RF) binary classifier (Fig. 1a). The best fitting (out-of-bag error rate=7.83%) was notably achieved during the training procedure with the following tuning parameters: number of trees=500 and feature subset size=33. Subsequently, features were ranked according to their importance based on the mean decrease of the Gini index, revealing the SYTO 14 signal (which stains RNA-rich regions), followed by 9 TL-related features (including 6 nuclear-specific parameters), as the main variables allowing for the recognition of transcription inhibition (Fig. 1c; Supplementary Material 1). Of note, feature-based hierarchical clustering of the entire compound set, weighted by RF, neatly separated transcription inhibitors (n=21, 8 of which are confirmed ICD inducers) from cytotoxic drugs that fail to inhibit transcription (n=64, among which only 2 have been reported to induce ICD), even though they were absent from the training set (Fig. 1d). In addition, SYTO 14 staining confirmed that the bright refringent structures identified through TL visually correspond to nucleoli. Altogether, these observations tend to highlight the specificity of the nucleus-related parameters as early markers of drugs inhibiting the transcriptional machinery.

AI models unboxing reveals nucleolar condensation as an indicative feature of transcriptional inhibition

The suppression of DNA-to-RNA transcription (linked to "dactinomycin-like" phenotype) is accompanied by morphological changes that can be captured by TL microscopy and automated analysis of the resulting images using convolutional neural network (CNN) model [29]. We used Gradient-weighted Class Activation Mapping (Grad-CAM) to visualize the cellular features that explain the deep learning decisions leading to the classification of drugs as "dactinomycin-like" [33, 34]. Grad-CAM images revealed that the neural network detected refringent subnuclear structures (usually 1–3 per nucleus) that were more compact in cells treated with transcriptional inhibitors that in untreated cells or cells treated with the topoisomerase II inhibitor etoposide, which does not inhibit transcription nor induces ICD [32, 35] (Fig. 2a). These subnuclear structures appear to be the same as the one detected by the RNA stain SYTO 14. We conclude that inhibition of DNA-to-RNA transcription correlates with the compaction of nucleoli, which concentrate ribosomal biogenesis and hence are particularly abundant in SYTO 14-stained RNA (Fig. 1b).

As the CNN recognition model was primarily trained using images from dactinomycin-treated cells, thus increasing risk of misclassification due to overfitting, it was refined with a larger set of micrographs from multiple cell lines treated with a panel of transcriptional inhibitors (Fig. 2b; Supplementary Material 2). Similarly, the model's specificity was enhanced by the automated recognition of dead cells, which do not manifest a discernible CON phenotype (Fig. 2b). This refined model was evaluated on both training (loss=0.32; accuracy=0.87) and validation (loss=0.33; accuracy=0.86) sets, showing (i) the good performance of the classifier and (ii) the absence of overfitting, the score pairs being very similar. Both model outputs similarly correlated with transcriptional inhibition, as measured by two different methods: the inhibition of fluorescent RNA precursor 5-ethynyl uridine (EU) incorporation into cells [36], as well as the separation of fibrillarin (FBL, a nucleolar marker) and nucleolin (NCL, which is released from the nucleolus when rRNA synthesis is inhibited) that can be detected by immunofluorescence [37, 38] (Fig. S1a-f). However, the refined model avoided misclassifying methotrexate as a transcription inhibitor and cisplatin as an inert compound (Fig S1a, c, e).

To further confirm that the refined model relied on nucleoli condensation for its recognition capabilities, we retrospectively applied the GradCAM technique to TL images from the Cell Painting assay (Fig. 1b). When the resulting heatmap was overlaid to SYTO 14 micrographs, it turned out that the image regions with the highest weights for the identification of the CON phenotype were overlapping with nucleoli (Fig. 2c).

In addition, we trained Generative Adversarial Networks (GANs) to generate synthetic images from white noise, simulating either inert cells or cells displaying the

CON phenotype. In the latter case, the trained network clearly generated 1–3 dense round structures, typically mimicking the CON phenotype (Fig. 2d). Of note, out of 100 synthetic images, 98 were properly classified as CON^-, while 91 were properly classified as CON^+ by the refined CNN model (Fig. 2e).

Holotomographic microscopy, a label-free laser technique visualizing the refractive index (RI) tomogram [39, 40], grants the possibility of precisely defining the contours of nuclei and nucleoli and quantifying the nuclear area occupied by nucleoli. This method allowed for the real-time detection of nucleolar condensation that was induced by transcriptional inhibitors but did not occur in untreated controls or etoposide-treated cultures (Fig. 2f-h).

We conclude that CON is a TL microscopy-detectable morphological correlate of transcriptional inhibition that can be potentially taken advantage of to screen drug libraries for the identification of compounds that interfere with DNA-to-RNA transcription.

Aclarubicin induces CON and ICD without early DNA damage

Anthracyclines such doxorubicin (DOXO) or the anthraquinone mitoxantrone (MTX), along with chemically unrelated compounds including dactinomycin (DACT), are prototypic ICD inducers that also suppress DNA-to-RNA transcription [30, 41]. In contrast to MTX, which like other classical anthracyclines is a potent DNA damaging agent (hence causing the phosphorylation of H2AX (γH2AX) detectable with a phospho-neo-epitope-specific antibody that recognizes serine 139-phosphorylated histone 2AX), aclarubicin (ACLA) does not damage DNA [42] and hence fails to induce γH2AX (Fig. 3a,c; Fig. S2a, b). In this assay, DACT yields a weaker DNA damage response than MTX, but a stronger effect than ACLA (Fig. 3a, c; Fig. S2a, b). However, similarly to MTX or DACT, ACLA does inhibit transcription measured by EU incorporation (Fig. 3b,c; Fig. S2c, d), FBL/NCL separation (Fig. 3c; Fig. S2e-g) or TL (Fig. 3c; Fig. S2h-j). Similar to the positive controls, the ICD inducers MTX [41] and oxaliplatin (OXA) [43], ACLA induced ICD hallmarks including the release of ATP (Fig. 3d) and HMGB1 (Fig. 3e) from cells, the exposure of CALR on the cell surface (Fig. 3f, g; Fig. S2k-m) and the induction of a Type-1 IFN response (Fig. 3h, i). Similarly, ACLA stimulated the immunofluorescence-detectable phosphorylation of eIF2α (on serine residue 51, which is hence lost upon its substitution to alanine) [44], which is pathognomonic of ICD [27] (Fig. 3j, k). In accord with these in vitro observations, ACLA-killed MCA205 fibrosarcoma cells injected subcutaneously (*s.c.*) into histocompatible, immunocompetent C57Bl/6 mice elicited an immune response that completely protected all animals (10 out of 10) against rechallenge with live MCA205 cells injected 1 week later into the opposite flank (Fig. 3l-n; Fig. S2n-p). When rechallenged for a second time with MCA205 cells, tumor-free mice vaccinated with either ACLA or MTX-treated malignant cells demonstrated resistance against tumor development (10/10 and 9/10, respectively) (Fig. 3o).

Nucleolar condensation without DNA damage is compatible with ICD

To further characterize the ability of compounds to induce ICD solely through CON, we performed a systematic screen on 274 drugs contained in the DNA/RNA synthesis library. U2OS cells were cultured for either 24 (to assess cell death) or 4 h in the presence of each compound to detect four parameters, namely, (i) cell death leading to cell loss, (ii) DNA damage-associated γH2AX, (iii) RNA synthesis reflected by EU incorporation and (iv) CON identified by TL microscopy (Fig. 4a, b; Fig. S3a), after having measured the autofluorescence of each drug (Fig. S4) to allow for suitable compensation of fluorescent parameters. In parallel, when available, information about drugs' enzymatic target and/or interaction type with DNA was automatically retrieved from the DrugBank database. Unsupervised hierarchical clustering of the drugs led to the identification of four different categories of cytotoxic drugs (Fig. 4b-f; Fig. S3a). The first "DOXO-like" category contains drugs that share the effects of prototypic anthracycline doxorubicin (DOXO) and hence induce DNA damage, inhibit RNA synthesis and trigger pronounced CON. This "DOXO-like" group is enriched in *bona fide* ICD inducers including several anthracyclines [27], DACT [30] and OXA [43]. The second "CDDP-like" group of drugs induces marked DNA damage, partial transcriptional inhibition and a weak CON phenotype as found for cis-diamminedichloroplatinum (II) (CDDP, best known as cisplatin). None of the drugs falling into this category has been considered as an ICD inducer. The third, "ETO-like" group tends to cause marked DNA damage but no or little inhibition of RNA synthesis and CON phenotype, like the prototypic non-ICD inducer etoposide (ETO). The final "ACLA-like" group is composed by agents that kill cancer cells without DNA damage (i.e., without H2AX phosphorylation) but tend to inhibit EU incorporation into cells and/or to induce the CON phenotype. Beyond aclarubicin (ACLA), this group contains confirmed ICD inducers such as lurbinectidin [23] and dinaciclib [45] (Fig. 4b; Fig. S3a).

The "ACLA-like" cluster includes an eclectic mix of 19 molecules that include several inhibitors of topoisomerase (II or unspecific, $n=5$) and RNA polymerase I ($n=4$). The "DOXO-like" group contains a majority of compounds (13 out of 15) that are classified as topoisomerase II (gyrase) inhibitors, while the "CDDP-like" group

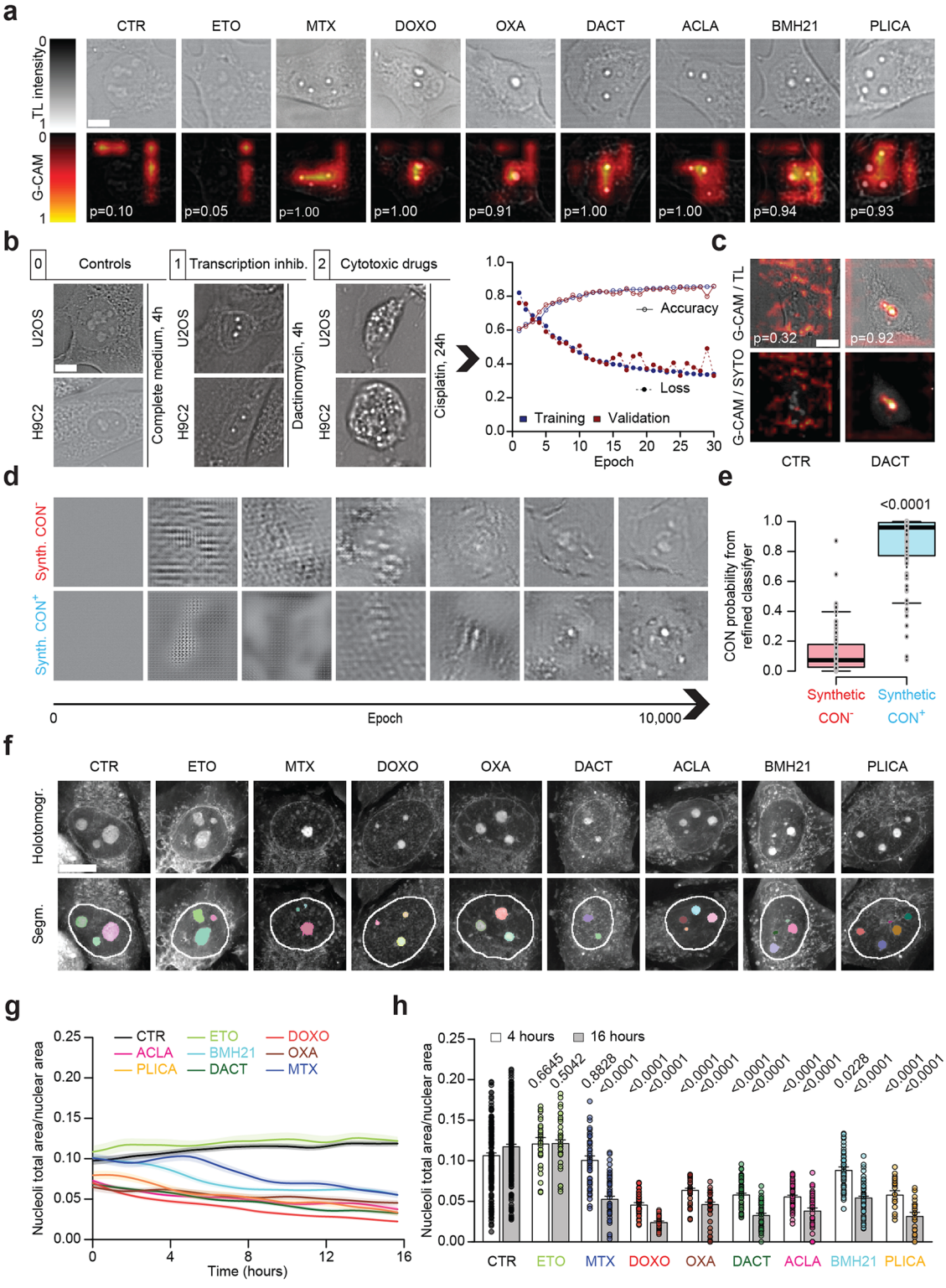

Fig. 2 (See legend on next page.)

(See figure on previous page.)

Fig. 2 Unboxing deep neural networks discloses condensation of nucleoli (CON) as utmost relevant subcellular phenotypic feature. (**a**) Human osteosarcoma U2OS cells were treated with a panel of chemical agents, i.e. 3 µM etoposide (ETO), 3 µM mitoxantrone (MTX), 3 µM doxorubicin (DOXO), 500 µM oxaliplatin (OXA), 3 µM dactinomycin (DACT), 15 µM aclarubicin (ACLA), 1 µM BMH21, 5 µM plicamycin (PLICA), or left untreated (CTR) for 4 h, imaged using transmitted light (TL) and representative images are displayed. After automated nuclei detection using semantic segmentation, patches were extracted, subsampled and then classified using trained Deep Convolutional Neural Network (DCNN). Gradient-weighted Class Activation Mapping (Grad-CAM) technique was used to map principal features from the final convolutional layer to the original image. The heatmap generated from Grad-CAM highlighting the crucial regions for the network's prediction is overlayed to the original TL image. Color represents the degree of activation (importance) from low (0, black), through medium (0.5, red), to high (1, yellow). The DCNN-predicted probability values (p) of condensation of nucleoli (CON) are superimposed on each image. (**b**) The initial DNN classifier was generalized by enriching the training set with additional micrographs of new cell types (e.g. H9C2) and various treatments (including cytotoxic agents). Left panel: Top numbers indicate the newly trained classes (0: controls; 1: early transcription inhibitors; 2: late cytotoxic drugs), exemplified by representative images from selected conditions. Right panel: the training process is depicted as the evolution of accuracy (plain dots) and loss (circles) along epochs. Blue and red colors represent the training and validation sets, respectively. (**c**) Manually selected regions of interest (ROI) from TL micrographs, generated in the Cell Painting assay (Fig. 1) after treatment with DACT or untreated (CTR), were resized and used to generate GradCAM images with the trained DCNN. These images were then overlayed to both original TL and SYTO 14-stained ROIs. The predicted probabilities (p) for CON induction are superimposed on each TL image. (**d**) Two generative adversarial networks (GANs) were trained to generate images of CON^- and CON^+ classes. Examples of image series belonging to the two classes synthesized by GANs are depicted over multiple epochs during the training process, ranging from 0 to 10,000. (**e**) Boxplots represent the CON probabilities calculated from the DCNN of a panel of images belonging to synthetic CON^- and CON^+ class generated by GANs. (**f**) U2OS cells were left untreated (CTR), or treated with 10 µM ETO, 3 µM MTX, 3 µM DOXO, 500 µM OXA, 1 µM DACT, 5 µM ACLA, 1 µM BMH21 or 5 µM PLICA and subsequently imaged via time-lapse holotomographic microscopy every 20 min for a total duration of ~ 16 h. Representative holotomographic images together with the segmentation overlay of the nucleus (in white) and of nucleoli (in different colors) are displayed. (**g**) Kinetics of total areas of nucleoli over that of nuclei are displayed as median ± MAD. (**h**) Nucleoli total area over nuclear area was extracted for 4 h and 16 h timepoints and represented in bar charts as median ± MAD with dots representing each segmented cell. P-values were calculated using pairwise Mann-Whitney test against adequate control. Scale bars represent 10 µm

contains a majority of drugs (10 out of 14) that inhibit topoisomerase I. This suggests that specific topoisomerase I inhibition cannot induce ICD, while topoisomerase II or RNA polymerase can do so. Curiously, the four most common platinum salts did not cluster altogether, despite their close chemical origin (Fig. S3a). As DMSO solvent was described as an inhibitor of the cytotoxicity of platinum compounds [46], we further tested three of them, dissolved in aqueous solution. While they all induced significant DNA damage, their ability to induce CON could be ranked from high to none (oxaliplatin > cisplatin > carboplatin) (Fig S3b, c). This result corroborates previous findings that classified oxaliplatin, cisplatin, and carboplatin as highly, partially and non- immunogenic, an observation that could be explained by their capacity to induce ribosome biogenesis stress in addition to DNA damage [47–49].

Intrigued by the "ACLA-like" group, which seems to uncouple DNA damage from transcription inhibition, we decided to select the well-described RNA synthesis inhibitors bisantrene, BMH21, CX5461 and plicamycin for further characterization. Validation experiments confirmed that all these agents induced nucleolar condensation over time in U2OS and HeLa cells, as determined by TL at endpoint (Fig. S5a, b) or by holotomography (Fig. S6), coupled to cytotoxic effects (Fig. S5c-e). In contrast, most of the selected inhibitors of DNA-RNA transcription (except for CX5461) induced no or little early DNA damage reflected by immunoblot or immunofluorescence detection of γH2AX (Fig. S5f-i). The selected transcription inhibitors were heterogeneous with respect to their capacity to induce histone eviction, which was measured as the reduction of the nuclear fluorescence of photoactivatable GFP-histone H2A fusion protein in photoactivated regions after drug exposure [50]. Thus, bisantrene and plicamycin induced little, but BMH21 and CX5461 considerable, histone eviction, though less than the positive controls DOXO [50] and ACLA [42] (Fig. 5a-d). Heterogeneous effects were also observed for bisantrene, BMH21, CX5461 and plicamycin with respect to the presence of non-mitochondrial double-stranded DNA (dsDNA) in the cytosol of cells (Fig. S7a, b), the type 1 interferon response (Fig. S7c, d) and eIF2α phosphorylation (Fig. S7e, f), although all these effects were significant as compared to untreated control cells.

In the next step, we tested the four transcriptional inhibitors that do not or partly elicit DNA damage for their capacity to induce ICD in vaccination experiments. For this, cutaneous fibrosarcoma MCA205 cells were treated with each of the drugs in vitro, washed and then injected orthotopically into immunocompetent, histocompatible C57Bl/6 mice. One week after this vaccination step the mice were rechallenged with live MCA205 cells injected into the opposite flank, and tumor growth was monitored. As compared to the positive controls, the confirmed ICD inducers ACLA and MTX, the transcriptional inhibitor could be ranked according to their capacity to delay or suppress tumor growth from high to low (CX5461 > BMH21 > bisantrene > plicamycin). However, all of them caused a significant delay in tumor growth and kept a significant percentage of mice alive and tumor-free (Fig. 5e, f; Fig. S8a-g). Tumor-free mice were resistant to rechallenge with MCA205 cells but remained permissive to the growth of antigenically unrelated B16-F10 melanomas (Fig. 5g, h), indicating that they had developed specific immunity. Hence, all transcriptional inhibitors

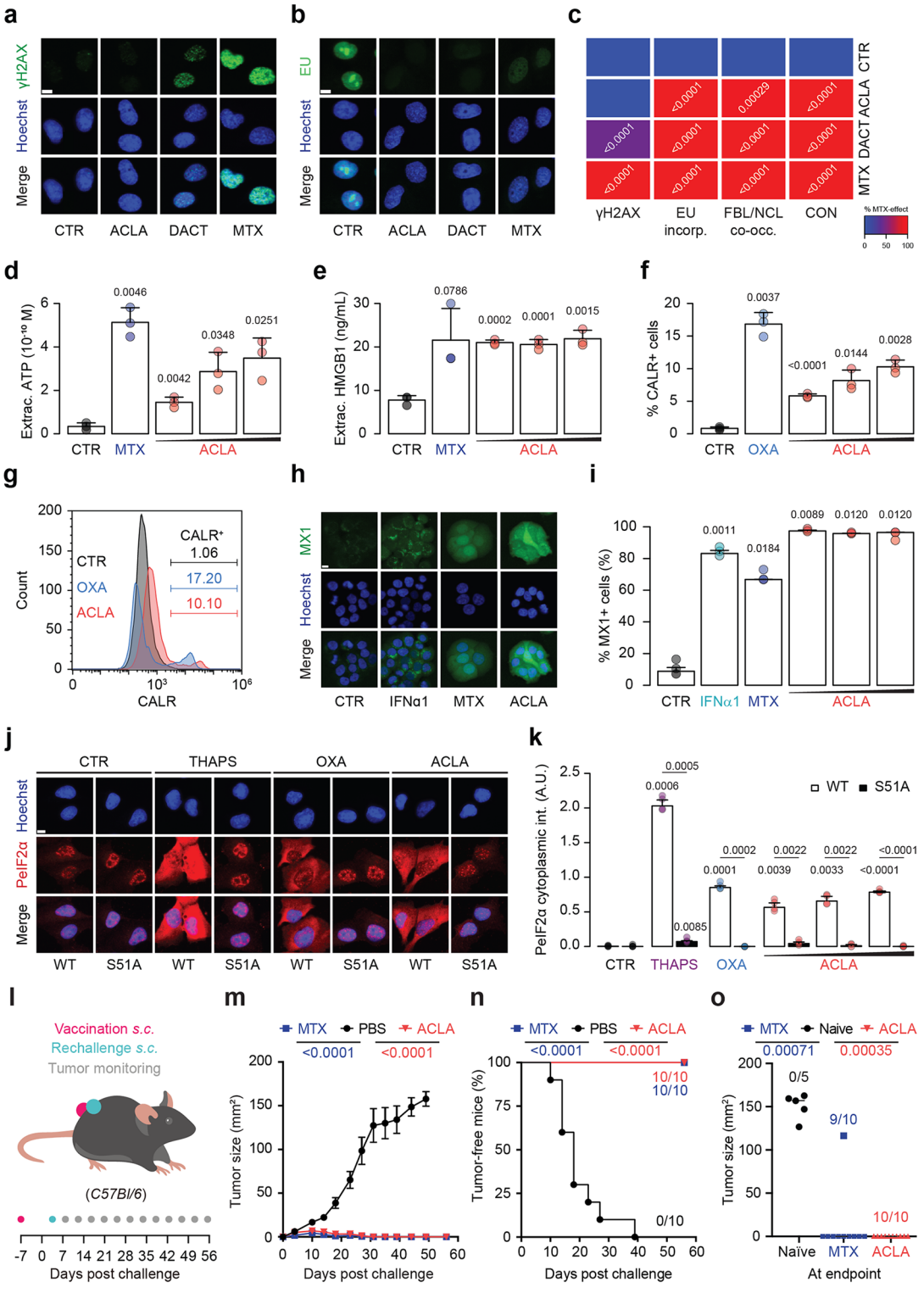

Fig. 3 (See legend on next page.)

are efficient ICD inducers. Accordingly, systemic treatment of mice bearing established tumors with BMH21 significantly reduced tumor progression, and this effect was lost upon in vivo depletion of T cells by monoclonal antibodies specific for CD4 and CD8. Hence, the anticancer effects of BMH21 fully depend on a T cell-mediated anticancer immune response (Fig. S8h-k).

(See figure on previous page.)

Fig. 3 Aclarubicin interferes with RNA synthesis, does not cause DNA damage and is immunogenic in cultured cells and in murine vaccination.(**a**) Human osteosarcoma U2OS cells were treated with 5 µM aclarubicin (ACLA), 1 µM dactinomycin (DACT), 3 µM mitoxantrone (MTX), or left untreated (CTR) for 4 h. After fixation, nuclear counterstaining with Hoechst 33342 and permeabilization, cells were further stained with anti-Phospho-Histone H2A.X (Ser 139) antibody, images were acquired by fluorescence microscopy and analyzed. Nuclear γH2AX intensity was quantified, and representative images are displayed. (**b**) U2OS cells were pre-treated as previously listed for 2.5 h and treatment pursued for 1.5 additional hours in the presence of 1mM 5-ethynyl uridine (EU). After fixation and nuclear counterstaining with Hoechst 33342, cells were permeabilized, EU was stained with an Alexa Fluor-488-coupled azide, images were acquired by fluorescence microscopy and analyzed. Nuclear EU intensity was quantified, and representative images are displayed. (**c**) H2AX phosphorylation (γH2AX) and EU incorporation were assessed as described above. To quantify the co-occurrence of fibrillarin (FBL) and nucleolin (NCL), U2OS cells were treated as previously listed for 4 h before fixation and permeabilization. Cells were then stained with the combination of a rabbit anti-fibrillarin and a mouse anti-nucleolin antibodies, followed by a staining with anti-rabbit Alexa Fluor-564-coupled and anti-mouse Alexa Fluor-488-coupled antibody, respectively. The CON phenotype was assessed using a trained Convolutional Neural Network (CNN) after automatically extracting nuclei images from TL micrographs through semantic segmentation. The effect of H2AX phosphorylation, EU incorporation, co-occurrence of FBL/NCL and CON phenotype from transmitted light (TL) was ranged between 0 and 100% of the effect of the positive control mitoxantrone (MTX) and values are summarized in an heatmap. (**d**) U2OS wild-type (WT) cells were treated with a dose range of ACLA (5 µM, 10 µM and 20 µM), with 2 µM MTX or 500 µM oxaliplatin (OXA) as positive controls or left untreated (CTR) for 24 h. The concentration of ATP secreted in the supernatant was quantified with a luciferase-based bioluminescence kit. (**e**) U2OS WT cells were treated as described above and the concentrations of HMGB1 released in the supernatant was quantified with a specific ELISA kit. (**f**) U2OS WT cells were treated for 6 h, medium was refreshed for additional 24 h and after collection, the surface-exposed calreticulin (CALR) was stained with a specific antibody. DAPI was used as an exclusion dye, cells were acquired by flow cytometry and the percentage of $CALR^+$ cells among viable ($DAPI^-$) ones is depicted. (**g**) Histograms representing CALR intensity are illustrated for each condition and percentages of $CALR^+$ $DAPI^-$ are reported. (**h**) U2OS WT cells were treated for 6 h and medium was refreshed for supplemental 24 h. Supernatants were transferred on HT29 MX1-GFP reporter cells for 48 h, and 100 ng/mL human type 1a interferon (IFNα1) was added as an additional positive control. Representative images are displayed. (**i**) The percentage of $MX1^+$ cells is reported in a bar chart. (**j**) U2OS WT and U2OS cells expressing non-phosphorylatable eIF2αS51A (S51A) were treated for 6 h with previously listed treatments, with the addition of 3 µM thapsigargin (THAPS) as positive control. The phosphorylation of eIF2α (PeIF2α) was assessed by immunofluorescence staining with a phosphoneoepitope-specific eIF2α antibody and representative images are displayed. (**k**) PeIF2α cytoplasmic intensity was quantified, and represented as a bar chart. (**l**) Experimental outline of prophylactic vaccination. Mouse fibrosarcoma MCA205 cells were treated in vitro with 15 µM ACLA or 4 µM MTX. Dying cells were harvested and subcutaneously (*s.c.*) injected into the left flank of immunocompetent syngeneic C57Bl/6 mice ($n=10$ mice per group), while the control group was injected with PBS. Ten days later, animals were rechallenged with living MCA205 cells in the contralateral flank of the mice and tumor size was regularly monitored. (**m**) The course of tumor volume curves is depicted. (**n**) Tumor-free survival is shown for each group. (**o**) ACLA- and MTX-vaccinated tumor free mice (ACLA $n=10$, MTX $n=10$) as well as naïve mice ($n=5$) were rechallenged by *s.c.* injection of living MCA205 cells in the right flank of the mice and tumor growth was monitored. The dot plot indicates tumor volumes at endpoint for each group. Values in bar charts are expressed as mean ± SD of one representative out of three independent experiments. Significant p-values for in vitro assays were determined by pairwise Mann-Whitney test versus relevant control. Values in tumor growth curves are expressed as mean ± SEM, and median of tumor sizes is reported for the endpoint dot plot with p-values calculated with pairwise Mann-Whitney test versus control. TumGrowth (https://github.com/kroemerlab) was used to analyze in vivo data. Statistical significance of tumor-free survival was calculated with log-rank test. Scale bars equal 10 µm

Finally, cardiac function and structure in mice subjected to chronic ACLA and BMH21 treatment were evaluated using echocardiography with speckle tracking to assess potential cardiotoxicity (Fig. S9a). ACLA-treated mice showed no signs of cardiotoxicity (Fig. S9b-h), in accordance with a previous study [42]. Despite a non-significant tendency towards lower ejection fraction and cardiac output, BMH21-treated mice preserved normal cardiac measures and exhibited comparable global longitudinal strain to both controls and ACLA-treated mice, indicating preserved contractility (Fig. S9b-h).

We conclude that transcriptional inhibitors that largely fail to cause DNA damage efficiently induce ICD. Accordingly, systematic correlation analyses showed that the CON phenotype, which reflects the suppression of DNA-to-RNA transcription, has the strongest relationship with vaccination efficacy ($R=0.94$), logically followed by nucleolar size ($R=0.89$) and eif2α phosphorylation ($R=0.72$). No significant association between vaccination efficacy, DNA damage, histone eviction, cytosolic dsDNA accumulation was detected (Fig. 5i, j).

Molecular descriptors fed into a neural network efficiently predict CON-inducing drugs

We screened ~ 5,000 compounds contained in several collections (Fig. 6b) to determine their capacity to induce the CON phenotype detectable by our trained CNN on TL microscopic images of paraformaldehyde-fixed cell cultures. Duplicated molecules across libraries were detected and removed by computing the Tanimoto distance matrix, thus leading to a training set of 2,968 unique compounds (Supplementary Material 3), among which 3.77% were classified as CON^+ (Fig. 6a, b). We then correlated the capacity of each compound to induce CON based on their molecular descriptors computed using the Chemistry Development Kit (CDK) ($n=287$ that were reduced to $n=116$ after elimination of low variation features) by means of three different AI procedures establishing quantitative structure–activity relationships (QSAR), namely, (i) neural network (NN), (ii) random forest (RF) and (iii) xgboost (XG). The performance of the three QSAR models was evaluated by means of the Monte Carlo cross-validation (MCCV, $n=10$) procedure using the NCI-mechanistic library as a validation set (654 unique molecules, among which 4.59% were classified as

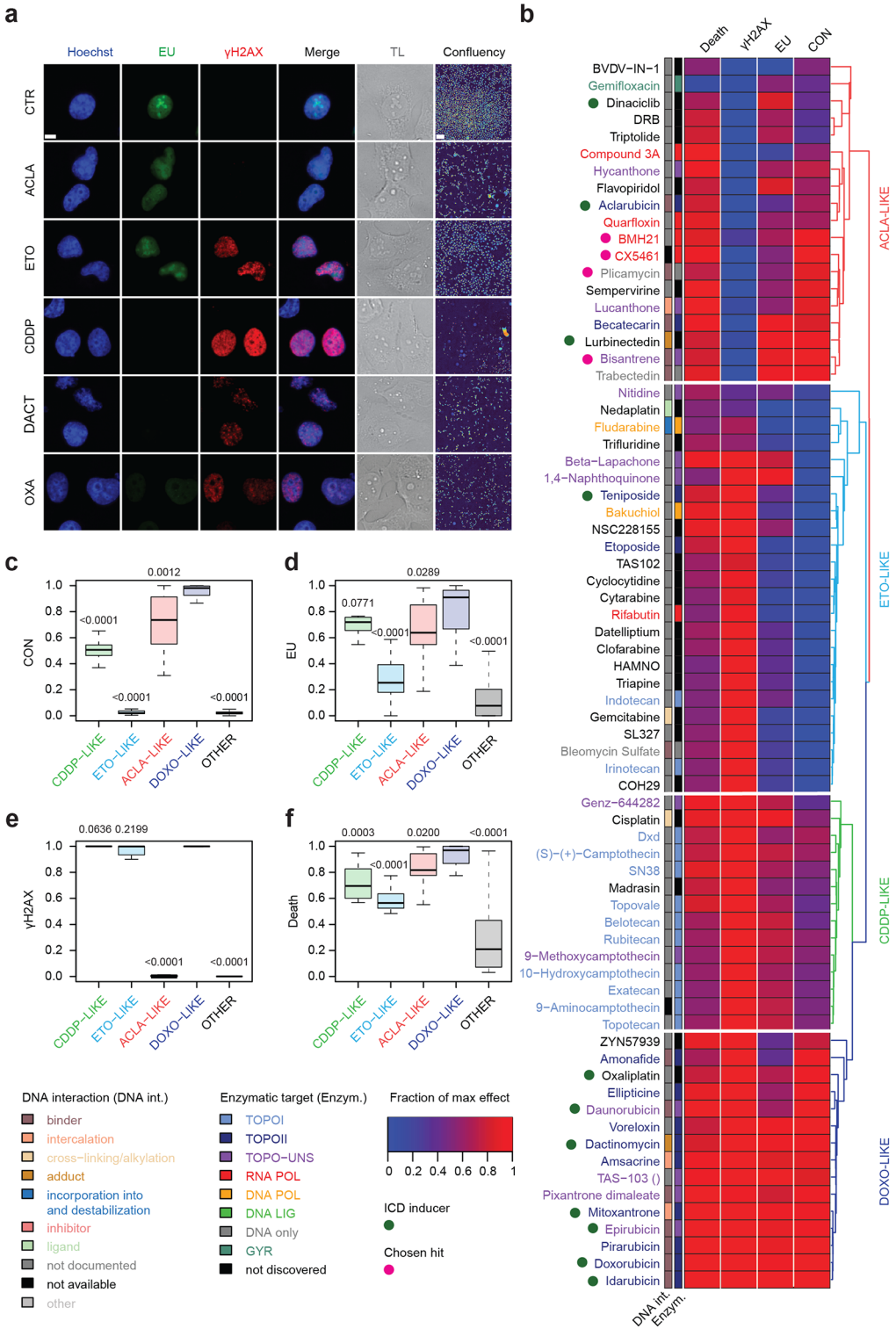

Fig. 4 (See legend on next page.)

(See figure on previous page.)

Fig. 4 Classification of drugs subtypes based on nuclear and toxicity features from a screening campaign. (**a**) Human osteosarcoma U2OS cells were pre-treated with a custom-made collection of 274 DNA/RNA-related drugs from TargetMol at 1µM, 10µM and 100µM or left untreated (CTR) for 2.5 h. Treatments pursued for 1.5 additional hours in the presence of 1mM 5-ethynyl uridine (EU). After fixation and nuclear counterstaining with Hoechst 33342, cells were permeabilized, EU was stained with an Alexa Fluor-488-coupled azide and cells were further stained with anti-Phospho-Histone H2A.X (Ser 139) antibody (γH2AX), followed by staining with Alexa Fluor 647 secondary antibody. To assess cell death U2OS cells were treated for 24 h, fixed and counterstained with Hoechst 33342. Images were acquired by fluorescence and transmitted light (TL) microscopy. Representative images of cells treated with 5 µM aclarubicin (ACLA), 10 µM etoposide (ETO), 300 µM cisplatin (CDDP), 1 µM dactinomycin (DACT), 500 µM oxaliplatin (OXA) or left untreated (CTR) are displayed. Scale bar equals 10 µm. A colormap representing confluency of cells is depicted for each condition. Scale bar represents 100 µm. (**b**) The clustered heatmap summarizes the fraction of maximum effects of each assessed parameter for 4 groups of interest (i.e. "ACLA-like", "ETO-like", cisplatin "CDDP-like" and doxorubicin "DOXO-like") at a chosen concentration that maximized the overall effect of the assessed parameters at 4 h. Cell death was quantified via enumeration of Hoechst-stained nuclei, DNA damage activity via nuclear H2AX phosphorylation (γH2AX), inhibition of transcription via EU intensity in the nucleus and condensation of nucleoli (CON) was evaluated by a trained convolutional neural network (CNN) applied to nuclei patches from TL images. Color-codes indicating DNA interaction (DNA int.) type and enzymatic target (Enzym.) are reported for each condition. TOPO, topoisomerase; UNS, unspecific; POL, polymerase; LIG, ligase; GYR, gyrase. Adjacent green dots highlight confirmed immunogenic cell death (ICD) inducers while rose red dots indicates hits chosen for further validations. Data of each group are also reported in boxplots, CON in (**c**), EU in (**d**), γH2AX in (**e**) and cell death in (**f**). P-values were calculated using a pairwise Mann-Whitney test against the "DOXO-LIKE" group for each assessed parameter

CON^+) (Supplementary Material 3) (Fig. 6c). The validation results were mainly represented by the Area Under the Curve (AUC) metric, which ranked the NN as the most accurate and stable model (medians: NN=0.89, RF=0.66, XG=0.82; median absolute deviations: NN=0.01, RF=0.11, XG=0.02) (Fig. 6d, left panel). In addition, confusion matrices were computed after determining the optimal probability cutoff that maximized the F1 score for each model, allowing for the calculation of several discrete metrics (Fig. 6d, right panel). AUC, Matthews correlation coefficient (MCC), and Balanced Accuracy (BA) were combined to compute a "performance score" that allowed to choose the best NN model among ten used for the cross-validation procedure. Of note, a Y-scrambling method applied to the NN model architecture showed that original models performed significantly better than "randomized" models (Fig. 6e), thus reinforcing our validation procedures.

To ensure the relevance of future predictions, we defined an applicability domain (AD) for our model as the confidence intervals stemming from the distribution of the individual distances d_{AD} to the normalized training set feature centroid (Fig. S10a, left panel). In the training set, 95% of the individuals had a distance d_{AD}<1.9, while the maximum distance reached was 6.0. It is worth noting than 95% of the compounds in the validation set had d_{AD}<2.0, while the maximum reached value d_{AD}=3.9 (Fig. S10a, top right panel).

In a final step, we used this NN-based QSAR algorithm to predict the ability of the ~320,000 compounds from the DTP NCI library (https://wiki.nci.nih.gov/display/NCIDTPdata/Chemical+Data) to induce the CON phenotype, from which 95% had d_{AD}<1.9, and 99% <6 (Fig. S10b, bottom right panel). Of note, all retrieved and computed compound information (descriptors, CON probability) were uploaded on a public open-access repository (https://github.com/kroemerlab/NucleolAI/tree/main/RESOURCES/NIH_320K). To highlight any potential enrichment in specific classes of compounds highly susceptible to induce CON, we automatically retrieved all the MeSH terms associated to each single molecule from the library, when available. After removing drugs already present in the training set, we ended with a collection of 10,948 MeSH records, out of 319,481 requests in total (3.4%). To exclude bias introduced by this drastic selection, we compared the distribution in CON probabilities of the subset versus the full dataset, using the Kolmogorov-Smirnov test. Although the p-value was significant due to the extremely large number of samples, the D metric, which quantifies the maximum distance between the two distributions, was relatively low (D=0.1), indicating a similar distribution of probabilities across the two sets (Fig. 6f). In total, 449 unique relevant MeSH terms were associated to the 10,948 records; after separating the compounds into two categories (p_{CON}≥0.98, n=167 and p_{CON}<0.98, n=10,777), we computed the occurrence of each term within them, which permitted to retrieve significant enrichments among putative CON inducers. This includes categories such as anthracyclines, naphthacenes as well as topoisomerase II inhibitors (Fig. 6g), which together represent the substance classes that include most known ICD inducers [4, 14, 17, 35]. Altogether, this enrichment analysis confirms the reliability of the NN-QSAR model, showing that in silico hits are associated with RNA synthesis inhibition.

Encouraged by these positive results, we attempted to track the molecular properties that determine the capacity of a drug to induce CON. To unlock this possibility despite the use of a "black box" model (Fig. S11a), we performed a Local Interpretable Model-Agnostic Explanations (LIME) analysis, which permitted to rank the different molecular descriptors as poor (score=0) or important (score=1) contributors. The 4 top contributors were identified as C3SP2, nAtomP, WTPT.5 and ALogp2 (Fig. S11b) which represent carbon connectivity for hybridization, the number of atoms in the largest pi chain, molecular branching and lipophilicity, respectively (Supplementary Material 4). This suggests that a

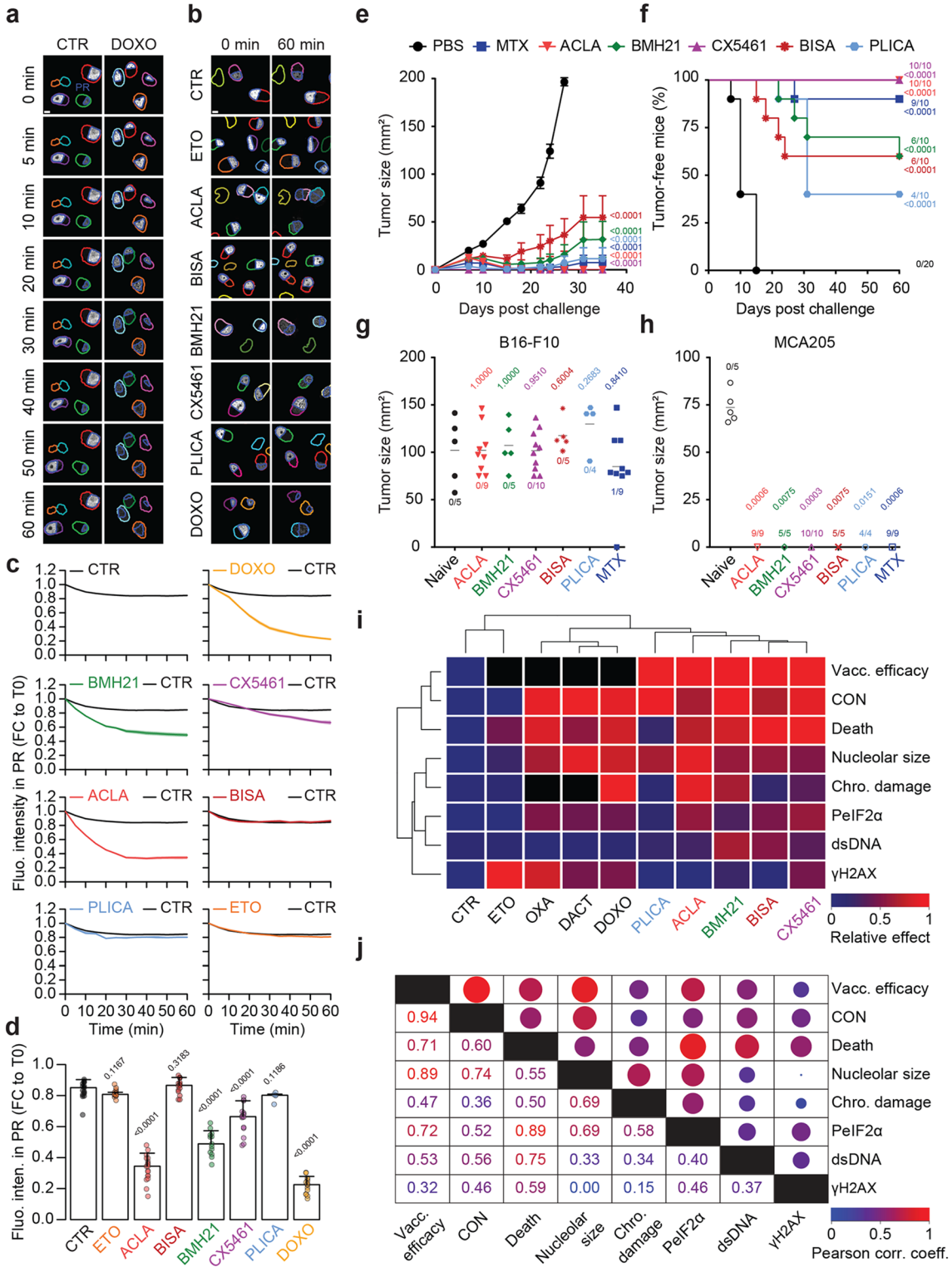

Fig. 5 (See legend on next page.)

(See figure on previous page.)

Fig. 5 Non-DNA-damaging agents are effective in prophylactic vaccination, which mostly correlates with condensation of nucleoli (CON) and cell death. (**a**) Human osteosarcoma U2OS cells expressing photoactivatable (PA)GFP-H2A were used to evaluate hits' chromatin-damaging activity after activation by laser of a portion of the nucleus. Segmentation of nuclei in colors (each color represents each nucleus that has been automatically tracked over time) and photoactivated region (PR) in blue are overlayed on representative cells treated with 10 µM doxorubicin (DOXO) or left untreated (CTR). Photoactivated PAGFP-H2A was subsequently monitored by time-lapse confocal microscopy for 60 min and tracked over time. (**b**) Partial nuclear photoactivation was performed as described above, cells were then treated with 10 µM etoposide (ETO), 10 µM aclarubicin (ACLA), 10 µM bisantrene (BISA), 10 µM BMH21, 10 µM CX5461, 5 µM plicamycin (PLICA), 10 µM doxorubicin (DOXO), or left untreated (CTR). Representative images of the first (0 min) and last (60 min) timepoint are displayed, with a segmentation overlay of nuclei in colors (each color represents each nucleus that has been tracked over time) and in the PR in blue. (**c**) Quantification of the fluorescence intensity of PAGFP-H2A in the PR expressed as fold change (FC) to the initial timepoint (T0) after each indicated treatment is reported over time. (**d**) Quantification of the fluorescence intensity of PAGFP-H2A expressed as FC to T0 in the PR after each treatment is reported in a bar chart corresponding to the last timepoint (60 min). Scale bars equal 10 µm. (**e**) Mouse fibrosarcoma MCA205 cells were treated in vitro with 4 µM mitoxantrone (MTX), 15 µM aclarubicin (ACLA), 5 µM BMH21, 15 µM CX5461, 10 µM bisantrene (BISA) or 50 µM plicamycin (PLICA). After harvesting, dying cells were subcutaneous (*s.c.*) injected into the left flank of immunocompetent syngeneic C57Bl/6 mice ($n=10$ mice per group), while the control group was injected with PBS. Ten days later, animals were rechallenged with living MCA205 cells in the contralateral flank of the mice and tumor size was regularly measured. The course of tumor volume curves is depicted. (**f**) Tumor-free survival is shown for each group. (**g**) Vaccinated tumor free mice (ACLA $n=9$, BMH21 $n=5$, CX5461 $n=10$, BISA $n=5$, PLICA $n=4$, MTX $n=9$) as well as naïve mice ($n=5$) were rechallenged by *s.c.* injection of living MCA205 cells in the left flank of the mice, with simultaneously *s.c.* injection of living mouse melanoma B16-F10 in the right flank. Tumor growth was monitored over time and tumor volumes at endpoint of each group are displayed in a dot plot for B16-F10, and in (**h**) for MCA205. Values in tumor growth curves are expressed as mean ± SEM, and median of tumor sizes are reported for the endpoint dot plot with p-values calculated with pairwise Mann-Whitney test versus control. TumGrowth (https://github.com/kroemerlab) was used to analyze in vivo data. Statistical significance of tumor-free survival was calculated with log-rank test. (**i**) The clustered heatmap summarizes the relative effect of each evaluated phenotype, i.e. vaccination efficacy (Vacc. efficacy), condensation of nucleoli (CON), death, nucleolar size, chromatin damage (Chro. Damage), phosphorylation of eIF2α (PeIF2α), dsDNA and γH2AX, assessed throughout the study for ACLA, BMH21, BISA, CX5461, PLICA, etoposide (ETO), oxaliplatin (OXA), dactinomycin (DACT), doxorubicin (DOXO) and the untreated (CTR) group. (**j**) A Pearson correlation matrix for the aforementioned effects is displayed. Pearson correlation coefficients are indicated in the lower triangular matrix, while being represented by circles whose size and color are mapped to their value in the upper triangular matrix

prototypical CON inducer exhibits high carbon connectivity, a large pi chain, significant molecule branching and low lipophilicity, as supported by the comparison of the relevant descriptors between CON^- and CON^+ molecules in the original training set (Fig. S11c).

Discussion

Various modalities of cancer treatment including cytotoxic drugs, targeted agents, antibody-drug conjugates, photodynamic therapeutics and oncolytic viruses are particularly efficient if they are capable of eliciting ICD of malignant cells. Indeed, the ICD-elicited immune response against tumor-associated antigens is crucial for prolonging therapeutic effects beyond treatment discontinuation. Moreover, ICD-inducing drugs can enhance the immune infiltration of initially scarcely infiltrated cancers rendering them "hot" and hence susceptible to immunotherapy with immune checkpoint inhibitors [4, 19, 51].

Mechanistically, ICD can be explained by the exposure and release of multiple DAMPs (including ANXA1, ATP, CALR, HMGB1, Type-1 IFNs) that act on pattern recognition receptors (PRRs) on immunocytes, setting off an immune response that involves dendritic cells and T lymphocytes. Logically, initial screening campaigns aiming at the discovery of ICD-inducing drugs were designed to measure the relocation of normally intracellular DAMPs to the surface or the extracellular space surrounding cancer cells. Since all these DAMPs are required for ICD [52], it appeared necessary to measure all of them in multiple parallel experiments and to explore only those hits as potential ICD inducers that were able to elicit the emission of all danger signals at once [21, 53, 54].

To simplify the procedure to identify ICD inducers, we investigated the mechanisms that underly the ICD-relevant emission of danger signals, thus discovering that one pathognomonic alteration that is essential for the premortem exposure of CALR as well as for the autophagy-dependent release of ATP, consisted in the phosphorylation of eIF2α [27]. However, this *sine qua non* phosphorylation lacks specificity, as conventional ER stressors such as thapsigargin can trigger such response without inducing ICD [27]. Moreover, the detection of eIF2α phosphorylation is based on immunofluorescence staining, precluding the use of robust biosensors and rendering it impractical for large screening campaigns. Subsequent molecular studies unraveled that most ICD inducers (with the notable exception of spindle poisons such as epothilones, taxanes and vinca-alkaloids) inhibit DNA-to-RNA-transcription upstream of eIF2α phosphorylation [30]. However, measurement of transcription is not easily scalable, again rendering impractical (or excessively costly) screening campaigns that would be based on the direct measurement of this parameter. For this reason, in this study, we attempted to develop an unbiased approach based on cellular morphology. Noteworthily, deep neural network-assisted analysis of transmitted light (TL) microscopic images trained for the detection of transcriptional inhibition was more efficient than a similar analysis of well more complex multicolor fluorescence images resulting from Cell Painting. TL-based image analysis identified nucleolar condensation as a morphological correlate of suppressed

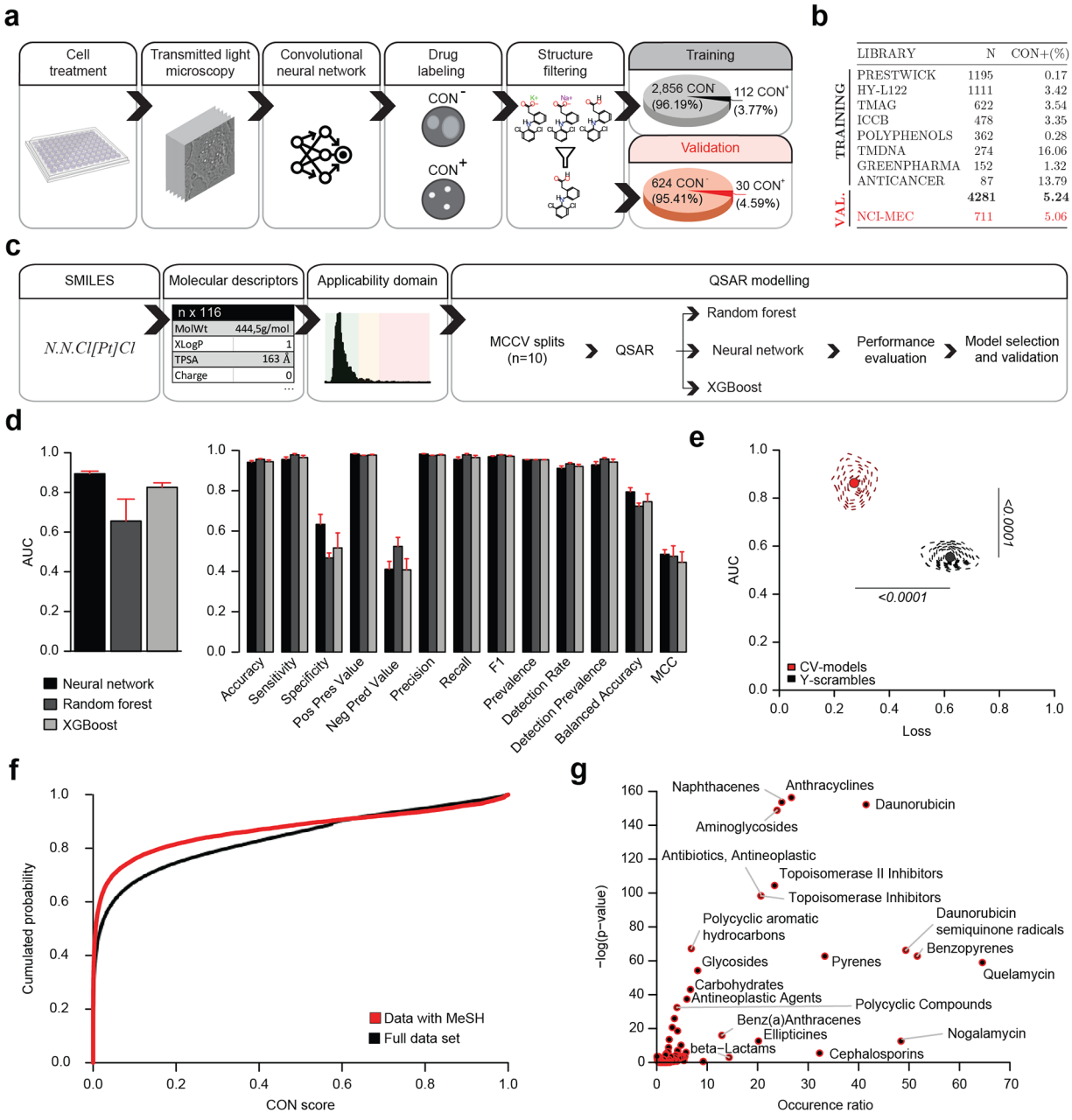

Fig. 6 (See legend on next page.)

DNA-to-RNA-transcription that then could be easily screened for the identification of novel ICD inducers.

Nucleolar condensation has previously been described in a variety of different contexts including, but not limited to, herpes virus infection of HeLa cells [55], acute cadmium intoxication of hepatocytes [56], the response of neurons to cerebral ischemia [57], cytomegalovirus infection of stromal cells from the bone marrow [58], oocyte cell death in atretic follicles [59], as well as in the initiation of mitosis [60, 61]. More interestingly for the context of this paper, nucleolar condensation has been observed in porcine oocytes treated with the transcriptional inhibitor dactinomycin [62, 63] or the protein synthesis inhibitor cycloheximide [62], as well as in HeLa cell treated with the ribosome synthesis inhibitor CX5461 [64]. Conversely, nucleolar size positively correlates with RNA polymerase I activity in liver regeneration [65], as well as in melanoma cells upon stimulation of ribosomal biogenesis by overexpressed Sik-similar protein (Sik-SP) [66]. Beyond these anecdotical reports, our studies suggest that any drug able to suppress transcription at a sufficient level causes nucleolar compaction detectable

(See figure on previous page.)

Fig. 6 Prediction of condensation of nucleoli (CON) through Quantitative Structure-Activity Relationship (QSAR) modelling using neural network and molecular descriptors. (**a**) The experimental outline for training set preparation is displayed. Human osteosarcoma U2OS cells were treated with the different libraries for 4 h. After fixation, images were acquired using transmitted light (TL) microscopy and extracted nuclei were classified by a convolutional neural network in condensation of nucleoli (CON) negative (CON^-) or positive (CON^+) phenotype. After a filtration step performed on the whole dataset based on Tanimoto similarity for duplicates removal, training and validation pies specify the number and corresponding percentage of CON^- and CON^+. (**b**) The libraries used in the screening campaign are presented in a table, each row specifying the library's name as described above, its number of compounds (N) and the percentage of compounds classified as CON^+. Libraries are further divided into training set in black and validation (VAL.) set in red. (**c**) The QSAR procedure is represented in a flowchart. Chemistry Development Kit (CDK) library was used for computing 116 descriptors of the compounds, some of which exemplified in a table. These descriptors were thereafter used to define an applicability domain and then fed to 3 different algorithms, i.e. natural network (NN), random forest and xgboost, for establishing a model capable to predict the CON phenotype. (**d**) Performance parameters statistics from the Monte Carlo cross-validation (MCCV) procedure of the different algorithms are reported. (**e**) Validation of the neural network model using y-scrambling procedure. The same NN model architecture was trained with 100 randomly shuffled training labels, and both loss and AUC were evaluated and reported in a bi-parametric plot. Dots represent the median for each group (black = y-scrambles; red = models from the initial cross-validation (CV) procedure). Dotted lined represent point densities. P-values calculated by means of the Mann-Whitney test against the MCCV original trainings' values are shown. (**f**) The ~320,000 compounds of the NCI database were annotated retrieving MeSH (Medical Subject Headings) terms. The predicted CON score was calculated with the neural network-based QSAR model previously trained. Cumulative distribution is plotted in black for the full data set ($n = 319{,}481$) and in red for data associated with MeSH terms ($n = 10{,}948$). (**g**) Compounds associated with MeSH records were split into two categories, according to their propensity to induce the CON phenotype, and the occurrence of each term (expressed as the fraction of compounds associated with it) was computed. The occurrence ratio and -log(p-value) from a χ^2 test between the two populations for each MeSH term are displayed in a biparametric graph

by transmitted light microscopy. The fine mechanisms explaining this effect remain elusive. However, it is worthwhile to note that the nucleolus is a membrane-less organelle delimitated by liquid-liquid and liquid-to gel phase transitions that depend on weak non-specific inter- and intra-molecular interactions of disordered polymers, intrinsically proteins and RNA [67–69], implying the abundance of each of these components may affect the size of nucleoli. In particular, polyanionic RNA species (such as starRNA, a class of unusually long untemplated RNA strand synthesized by terminal nucleotidyl-transferase 4b), determine nucleolar size [70]. Intriguingly, phase transitions affect the subnuclear distribution of fibrillarin, which is evinced from nucleoli upon transcriptional inhibition [71], as well as that of HMGB1, which plays an essential role in ICD [72].

We observed that drugs that inhibit DNA-to-RNA transcription cause nuclear compaction (measured in vitro) and ICD (determined by mouse experimentation) irrespective of their capacity of inducing DNA damage. This may be clinically important, because many of the side effects of anticancer drugs have been attributed to unwarranted DNA damage inflicted to normal cells [73, 74]. Moreover, improved DNA repair has been invoked as a common resistance mechanism against DNA damaging cytotoxicants [75, 76]. Based on our results, it may be worthwhile to screen anticancer drugs for their capacity to inhibit RNA synthesis (and hence to cause nucleolar size reduction and ICD) as a positive feature but to exclude compounds that cause DNA damage from further drug development. This approach would yield relatively non-toxic ICD inducers as a novel category of anticancer agents, in line with the non-cardiotoxic and immunostimulatory drug BMH21 introduced in the present work.

In a final twist, we correlated nucleolar compaction determined by image analyses of TL images with the molecular descriptors of drugs. Our analyses suggest that deep neural networks are particularly efficient in yielding a validated algorithm that predicts the capacity of a compound to elicit nucleolar condensation in silico. We have applied this algorithm to a list of 320,000 compounds and provide the results of the calculations as an opensource database (https://github.com/kroemerlab/NucleolAI/tree/main/RESOURCES/NIH_320K). We anticipate that the use of such an AI-based approach might accelerate drug screening campaigns by focusing on those compounds for which a high probability of ICD-inducing capacity has been computed.

Conclusions

This study highlights the condensation of nucleoli (CON) as a pivotal morphological characteristic of transcriptional inhibition. Leveraging AI-driven image analysis, we demonstrate that CON can serve as a readily identifiable biomarker for immunogenic cell death (ICD), even in the absence of DNA damage. By integrating this innovative screening approach with quantitative structure-activity relationship (QSAR) modeling, we have developed and validated a predictive model that accurately forecasts the propensity of molecules to induce CON based on their 2D chemical structure. The confluence of these methods offers a robust, novel, and cost-effective strategy for identifying ICD-inducing compounds. Moreover, our findings demonstrate that transcriptional inhibitors, such as aclarubicin, bisantrene and CX5461, are efficacious in inducing ICD, stimulating anti-tumor immune responses, and displaying potential for combination with immunotherapies. Importantly, this study underscores the significance of targeting transcription rather than relying solely on DNA damage, thereby expanding the therapeutic landscape of ICD inducers for cancer treatment. This work does not only provide novel insights into the molecular mechanisms underlying ICD but also presents a robust

screening tool for drug discovery, with significant implications for the development of safer and more effective cancer therapies.

Materials and methods

Cell lines and cell culture

Human osteosarcoma U2OS cells, human neuroglioma H4 cells, rat embryonic myocardium H9C2 cells, murine colon carcinoma CT26 and murine melanoma B16-F10 cells were purchased from the American Type Culture Collection (ATCC). Mouse fibrosarcoma MCA205 cells were obtained from Merck. Human colon carcinoma HT29 MX1-GFP, in which GFP is under the control of the MX1 promoter, as well as U2OS eIF2αS51A bearing a mutant non phosphorylatable version of eIF2α and co-expressing RFP-LC3, were generated by our team in the past [22, 30]. U2OS stably expressing histone H2A tagged with photoactivatable (PA) green fluorescent protein (PAGFP-H2A) were obtained from P.-A. Vidi (Integrated Center for Oncology, Angers, France) [77]. HeLa cells used for holotomography experiments were provided by Nanolive (Ecublens, Switzerland).

Cell lines were cultured in Dulbecco's Modified Eagle Medium (DMEM) and HT-29 MX1-GFP were cultured in McCoy's 5A media, both supplemented with 10% fetal bovine serum, 1% non-essential amino acids, 1% HEPES under standard cell culture conditions (5% CO_2, 37 °C) in a water-saturated atmosphere within a cell culture incubator (HeraCell, Heraeus, Germany). For HT-29 MX1-GFP cells, the culture medium was supplemented with 2 µg/mL puromycin. DMEM, McCoy's 5A and all supplements were purchased from Thermo Fisher Scientific (Carlsbad, CA, USA). Cell culture plastic supplies were purchased from Corning (NY, USA). Imaging plates were purchased from Greiner Bio-One (Kremsmünster, Austria) and Ibidi (Gräfelfing, Germany).

All cell lines were let adapt one week after thawing and maintained in culture for a maximum of 15 passages. Contaminations were regularly checked with the MycoStrip Mycoplasma Detection Kit (rep-mysnc-100) obtained from Invivogen (Toulouse, France).

Chemical libraries and drugs

The anticancer library was custom-arrayed by our group in the past [27]. The custom-designed library targeting DNA/RNA synthesis (LC00-CUST), the Autophagy Compound Library (L3200) and the Polyphenolic Natural Compound Library (L6100) were purchased from TargetMol (Boston, MA, USA); the FDA-Approved Anticancer Drug Library (HY-L122) from MedChem Express (Monmouth Junction, NJ, USA); the ICCB Known Bioactives Library from Enzo Biochem (Farmingdale, NY, USA); a custom-made selection of Natural Compound library (GPNCL) was obtained from Greenpharma (Orléans, France); the Prestwick Chemical Library from Prestwick Chemical (Illkirch, France); the NCI Mechanistic Diversity Set was kindly provided by the National Cancer Institute.

Aclarubicin (sc-200160), idarubicin hydrochloride (sc-204774A) were purchased from Santa Cruz Biotechnology; 5,6-Dichloro-1-beta-D-ribofuranosylbenzimidazole (DRB) (287891), dactinomycin (A1410), mitoxantrone (M6545), etoposide (341205), thapsigargin (T9033), doxorubicin (D1515), epirubicin hydrochloride (E9406), flavopiridol hydrochloride (F3055), triptolide (T3652) came from Sigma Aldrich (St. Louis, MO, USA); BMH21 (HY-12484), CX5461 (HY-13323), bisantrene dihydrochloride (HY-100875 A), trabectedin (HY-50936), plicamycin (HY-A0122) from MedChem Express (Monmouth Junction, NJ, USA); metarrestin (T12006), abemaciclib (T2381) from TargetMol (Boston, MA, USA); lurbinectedin (PM01183) from PharmaMar (Madrid, Spain), oxaliplatin (3400957954642), carboplatin (3400957255879) from Accord Healthcare (Ahmedabad, India). Becatecarin (101524), topotecan (609699) were kindly provided by the National Cancer Institute (NCI).

Reagents, stains and kits

Hoechst 33342 (H3570), SYTO™ 14 Green Fluorescent Nucleic Acid Stain (S7576), MitoTracker Deep Red (M22426), Concanavalin A/Alexa Fluor 488 conjugate (C11252), Phalloidin/Alexa Fluor 568 conjugate (A12380), 6-diamidino-2 phenylindole dihydrochloride (DAPI) (D1306), RIPA buffer (89901), Pierce protease inhibitor (A32955), Pierce phosphatase inhibitor (A32957), NuPAGE® LDS sample buffer 4X (NP0007), NuPAGE® sample reducing agent 10X (NP0009), NuPAGE® MOPS SDS Running buffer (NP0001) and Pierce™ BCA Protein Assay Kit (23225) were purchased from Thermo Fisher Scientific. Formaldehyde (F8775), Triton X-100 (T8787), Tween®20 (P1379) were purchased from Sigma Aldrich. Methanol (14262) came from Honeywell (Charlotte, North Carolina, USA). Tris-glycine 10X (EU0550), Tris buffered saline (ET220-B) and Bovine serum albumin (04-100-812) came from Euromedex (Souffelweyersheim, France). IFNα1 (752802) was purchased from BioLegend (San Diego, CA, USA).

Click-iT™ RNA Alexa Fluor™ 488 or 594 HCS Assay kits (C10327, C10330) were purchased from Thermo Fisher Scientific. ENLITEN ATP Bioluminescence Detection Kit (FF2000) came from Promega (Madison, MI, USA). HMGB1 Express ELISA kit (30164033) was obtained from Tecan (Lyon, France). ECL™ Prime western blotting detection reagents (RPN2236) were purchased from Cytiva (Marlborough, MA, USA).

Antibodies

Rabbit polyclonal phospho-histone H2A.X (Ser139) antibody (2577) used 1/500 was purchased from Cell Signaling. Rabbit polyclonal antibody against fibrillarin (ab5821) used 1/2,000, mouse monoclonal antibody against nucleolin (ab13541, clone 4E2) used 1/4,000, rabbit polyclonal antibody against calreticulin (ab2907) used 1/100, rabbit monoclonal antibody against phospho-eIF2α (Ser51) (ab32157, clone E90) used 1/500, mouse monoclonal beta Actin antibody (ab6276, clone AC-15) used 1/20,000 were purchased from Abcam (Cambridge, UK). Mouse monoclonal dsDNA marker antibody HYB331-01 (sc-58749) used 1/300 was obtained from Santa Cruz Biotechnology (Dallas, Texas, USA).

Anti-rabbit and anti-mouse AlexaFluor™ 488- (A11008 and A11029, respectively), anti-rabbit 568- (A11036) and anti-rabbit 647- (A21245) labeled antibodies used 1/1,000 were purchased from Thermo Fisher Scientific. Goat anti-rabbit IgG (H+L) horseradish peroxidase (HRP)-labeled secondary antibody (4050-05) used 1/10,000 came from Southern Biotech (Birmingham, AL, USA).

Depleting antibodies for in vivo experimentation anti-CD4 (BE0003-1, clone GK1.5) and anti-CD8a (BE0061, clone 2.43) were purchased from BioXcell (West Lebanon, NH, USA).

Fluorescence microscopy and image acquisition

One day before treatment, U2OS WT, U2OS eIF2αS51A expressing RFP-LC3 or MCA WT were seeded in 384-well μClear imaging plate and let adhere. The next day, cells were treated to assess eIF2α phosphorylation (PeIF2α) [78] at 6 h, DNA damage detecting phosphorylated histone H2AX (γH2AX) at 4 h, transcription by co-occurrence of fibrillarin (FBL) and nucleolin (NCL) [79] at 4 h, cytosolic double-stranded DNA (dsDNA) [80] at 4 h, or to monitor viability in live timelapse imaging over a 24 h period.

Cells were fixed with 3.7% formaldehyde containing 1 μg/mL Hoechst 33342 for 30 min at room temperature and fixative was exchanged to PBS. To perform the immunostaining of γH2AX, FBL and NCL, cells were permeabilized with 0.1% Triton X-100 for 10 min and unspecific antibody binding was blocked by incubation with 2% BSA for 1 h at room temperature. The primary antibody was incubated at 4 °C on a shaking rocker overnight, then cells were repeatedly washed with PBS, stained with AlexaFluor™ 647 (or 488, or 568)-coupled secondary antibody for 2 h at room temperature. Additional washing steps with PBS were performed before the automated acquisition. Detection of non-mitochondrial dsDNA required a live staining with 0.5 μM MitoTracker Deep Red half an hour before the end of the treatment and staining procedure followed a published protocol [80].

Images were acquired using the automated confocal microscopes IXM-C or HT.ai (Molecular Devices, Sunnyvale, CA, USA) equipped with either an Aura II light source (Lumencor, Beaverton, OR, USA) or an LDI-NIT laser illuminator (89 North, Williston, VT, USA), adequate emission and excitation filters (Semrock, Rochester, NY, USA), an Andor Zyla camera (Belfast, Northern Ireland), and a 20X, 60X PlanAPO or 40X WI objective (Nikon, Tokyo, Japan). The atmospheric environment used for live cellular imaging was controlled by means of an Ibidi gas mixer (Gräfelfing, Germany) or an FC-9 apparatus (Live Cell Instrument, Namyangju-si, Republic of Korea). Unless otherwise specified, at least 4 view-fields were captured for each well during the acquisition procedure.

Image processing procedures

The micrographs were segmented using freely available R software (https://www.r-project.org/), integrated with the *EBImage* [81] and *RBioformats* packages from the Bioconductor repository (https://www.bioconductor.org), as well as the *MetaxpR* and *MorphR* package from the Kroemerlab repository (https://github.com/kroemerlab). In broad terms, for generic fluorescence experiments, the nuclear signal (e.g.: from Hoechst 33342 dye) was used for defining nuclei regions, after subtracting the image background (retrieved from gaussian blur) and applying an adaptive threshold to the result. Nuclei were then separated and labeled using watershed operation. When required, cytoplasmic signal was detected following the same global procedure, using the Voronoi propagation method, with nuclei mask as a seed, for labelling. Subcellular compartments (notably in cell painting assay) were detected by applying a top hat filter with appropriate kernel size (Supplementary Material 5), followed by an adaptive thresholding procedure after a sigmoid transform with an adequate z center value (Supplementary Material 5). The obtained masks were thereafter used for computing cell features, such as signal intensity (e.g. γH2AX, Hoechst 33342, DAPI, 5-ethynyl uridine (EU) in nuclei, PeIF2α in cytoplasm), morphological parameters (e.g. area, length, centroid), or textural parameters (haralick). The full nomenclature of these parameters can be retrieved from the *EBImage* package documentation. For label-free semantic image segmentation (notably on TL micrographs), *keras* and *tensorflow* R packages were used, enabling the possibility to apply pre-trained Fully-Convolutional Neural Networks (FCNN) to the images for obtaining nuclei and cytoplasm masks, as previously described [29]. In most cases, prior statistical evaluation, debris and dead cells were discarded based on their size and shape, and the number of quantifiable cells in each image was retained for quality control (QC) evaluation and/or cell viability assessment.

Phenotypic profiling via cell painting assay

A phenotypic profiling of cellular organelles to examine morphological responses to chemical treatments was performed using an adapted "Cell painting" procedure [31]. Organellar labeling included the nucleus, nucleoli, endoplasmic reticulum, mitochondria and actin cytoskeleton. One day before treatment, U2OS cells were seeded in 384-well µClear imaging plates and let adhere. The next day, cells were treated with 3 µM of the anticancer library custom-arrayed by our group in the past [27], supplemented with a selection of transcription inhibitors (i.e. epirubicin, idarubicin, abemaciclib, becatecarin, trabectedin, BMH21, CX5461, aclarubicin, lurbinectedin, topotecan, metarrestin, DRB, flavopiridol, triptolide) for 4 h. Half an hour before the end of the treatment, cells were live-stained with 0.5 µM MitoTracker Deep Red, followed by a fixation step with 3.7% formaldehyde containing 1 µg/ml Hoechst 33342. Cells were permeabilized with 0.1% Triton X-100 and washed before staining with the remaining labeling reagents (5 µg/mL Phalloidin Alexa Fluor™ 568 conjugate, 100 µg/mL Concanavalin A Alexa Fluor™ 488 conjugate and 3 µM SYTO 14 green fluorescent nucleic acid staining) diluted in 1% bovine serum albumin (BSA) in 1X HBSS solution for 30 min. After a final washing step, automated image acquisition and segmentation were performed as described above. Of note, prior to segmentation, SYTO 14 images were preprocessed by subtracting 75% of Phalloidin signal, this last channel "leaking" into the first one. For each channel, a full panel of cellular and subcellular features (basic, shape, moment, haralick [82]) was thereafter computed for the next steps of the analysis. From 2,886 raw features, 577 were considered as relevant (i.e. uncorrelated), and used to generate two cellular subsets: (i) cells left untreated (n=43,903) and (ii) cells treated with transcription inhibitors (n=18,488). After balancing the two datasets by random subsampling (n=10,000), they were used to train a random forest (RF) binary classifier using R *caret* package, which automatically performs fine tuning (feature subset size) of the model. Variables (i.e. features) were then attributed an importance value by computing their mean Gini index decrease (Supplementary Material 1). These values were finally utilized as weights for computing pairwise Gower's similarity coefficient of compounds (each of them linked to a set of 577 feature averages), allowing to perform Hierarchical clustering.

Detection of global RNA transcription by 5-ethynyl uridine (EU) incorporation

Global RNA transcription was analyzed by measuring the incorporation of Click-iT chemistry-detectable 5-ethynyl uridine (EU) following an optimized version of the manufacturer's instructions [79]. Briefly, U2OS cells were cultured in 384-well µClear imaging plates, after 24 h cells were pre-treated for 2.5 h and the treatment was pursued in the presence of 1 mM EU for 1 h. After fixation with 3.7% formaldehyde supplemented with 1 µg/ml Hoechst 33342 for 1 h and permeabilization with 0.1% Triton X-100 for 10 min, Alexa Fluor-488 (or 594)-coupled azide was added for 2 h in the dark at room temperature. Multiple washing steps with PBS were performed before acquisition as previously described. The green (or red) fluorescence intensity corresponding to the EU amount in the nucleus was quantified as detailed above. Inhibition of transcription was calculated by ranging the GFP intensity in each condition between its value in untreated cells (0% inhibition) and its value in cells treated with the positive control dactinomycin (DACT) (corresponding to 100% inhibition).

Systematic screen

Human osteosarcoma U2OS cells were pre-treated with a custom-made collection of 274 drugs targeting DNA/RNA synthesis from TargetMol at 1 µM, 10 µM and 100 µM, or treated with 300 µM cisplatin, 500 µM oxaliplatin, 5 µM aclarubicin, 5 µM plicamycin or left untreated (CTR) for 2.5 h. Treatments pursued for 1.5 additional hours in the presence of 1mM 5-ethynyl uridine (EU). After fixation and nuclear counterstaining with Hoechst 33342, cells were permeabilized, EU was stained with an Alexa Fluor-488-coupled azide and cells were further stained with anti-Phospho-Histone H2A.X (Ser 139) antibody (γH2AX), followed by staining with Alexa Fluor 647 secondary antibody. Detailed procedures for EU incorporation and immunostaining are described above. As the library included many polycyclic compounds with fluorescent properties, we established quantitative autofluorescence models to systematically correct measurement drifts with the assessed dyes. Briefly, the same treatment procedure was applied using the entire drug collection, omitting cell staining. After acquisition, nuclei and cytoplasm masks were obtained from transmitted light (TL) images using semantic segmentation, and used to evaluate the average intensity in both compartments, as well as in background. This permitted to express the autofluorescence in each channel, as a percentage increase of background intensity, thereafter fitted to drug concentrations using a 4-parameters Log-Logistic function. The obtained fits were finally used to predict and subtract autofluorescence from stained images. To assess cell death, U2OS cells were treated for 24 h, fixed and counterstained with Hoechst 33342. Images were acquired by fluorescence and TL microscopy and analyzed as described above. As drug effects were evaluated using increasing concentrations, we chose to reduce the results to a single relevant dose. This step was achieved by selecting the dose at which the global effect at 4 h (i.e. the pondered sum) was maximized, while ensuring that

no major lethal effect was triggered (Cell number $N_{drug\_i} > 0.5xN_{CTR}$). The fraction of maximum effect was then computed for each parameter ranging from 0 (minimum effect) to 1 (maximum effect). In addition, when available, information records indicating (i) drug enzymatic target and/or (ii) interaction with DNA were retrieved from the library provider, DrugBank and/or MeSH databases using the PubMed PUG REST API (https://pubchem.ncbi.nlm.nih.gov/docs/pug-rest) (Supplementary Material 6).

Cell classification and computer vision using convolutional neural networks (CNN)

All described methods apply to transmitted light (TL) label-free micrographs, and were used to classify cell images in relevant categories. In a first step, nuclei were detected and filtered using the methods described above. After centroids extraction, single cell patches were generated and fed to a pre-trained CNN which evaluated its probability of belonging to a given class. Two different CNNs were used in the present study: (i) The "DACT-like" binary classifier, described in a previous work [29]; (ii) The "CON" classifier, an updated version of the first one, refined by increasing the training set heterogeneity and predicting 3 categorical probabilities, i.e. "normal", "CON", and "dead" phenotypes. Briefly, the initial training set was enriched with micrographs ('patches') of various cell lines (U2OS, H9C2, H4, CT26) that were either left untreated (class 0), or treated with transcriptional inhibitors (namely dactinomycin, mitoxantrone and oxaliplatin) for 4 h (short time, class 1), and also various cytotoxic agents for 24 h (long time, class 2). Of note, cell patches from class 2 were filtered by DAPI live staining, which allowed to detect dead cells, even in untreated conditions. Altogether, a total of 26,559 cell patches was generated and labeled (Supplementary Material 2) to be split into training (n=21,248) and validation (n=5,311) sets. The CNN was trained using the Adam optimizer (LR=10^{-4}), using categorical accuracy as evaluation metric and categorical cross-entropy as loss function, with 30 epochs. The GradCAM technique [34] was applied to these CNNs, using a selection of patches, to highlight important regions allowing for classification. As for model training, these patches correspond to TL micrograph crops stemming from cell treated for 4 h with transcriptional inhibitors.

Generative Adversarial Networks (GANs) [83], which allow for the generation of purely-synthetic images from Gaussian noise, were trained using a subset of patches that were fed to the CON classifier for training. Two independent generative models were created by training the first model with 3,616 CON^- patches and the second with 3,718 CON^+ patches. The iterative training process required 10,000 epochs for reaching reasonable convergence of the binary accuracy (the evaluation metric) and binary cross-entropy (the loss function) of both generator and discriminator components from the two models. Each output from the generators (set to generate 100 samples) was saved, to visually follow the learning phase over time.

Holotomographic microscopy

U2OS or HeLa cells were seeded in LIVE96 plates (Nanolive, Ecublens, Switzerland) and let adhere overnight. Immediately after treatment, live cell time-lapse images were captured every 30 min over 17 h using a 3D Cell Explorer 96focus microscope (Nanolive) equipped with an environmental controller, a dry 60X objective and USB 3.0 CMOS Sony IMX174 sensor. The acquired quantitative phase images were segmented using a pre-trained DCNN as described above, and the nucleoli total area over the nuclear area was quantified. Data were reduced by computing medians and MAD at each timepoint, and smoothened over time using a spline fit for kinetics assessment.

Assessment of ATP secretion

U2OS cells were seeded in 96-well plates and after overnight attachment, cells were treated for 24 h. Cell culture supernatants were collected and after centrifugation to remove cell debris, they were transferred to a white/clear bottom plate in order to quantify ATP using the ENLITEN ATP Bioluminescence Detection Kit. After the addition of enzyme and substrate, as well as ATP standards and water as blank, the ATP-dependent substrate conversion was measured by reading luminescence at 560 nm in a Victor spectrophotometer plate reader (PerkinElmer, Waltham, Massachusetts, USA). ATP concentrations were calculated using four-parameter logistics based on the standard curve.

Quantification of HMGB1 release

U2OS cells were seeded in 96-well plate, let adhere overnight and treated for 24 h. HMGB1 released in the cell culture supernatant was quantified using a sandwich ELISA following the manufacturer's instructions. Absorbance at 450 nm was assessed using a Victor spectrophotometer plate reader and HMGB1 concentrations were calculated using four-parameter logistics based on the standard curve.

Evaluation of calreticulin exposure

U2OS cells were seeded in 96-well plate and let settle overnight prior to treatment for 16 h. Cells were collected and ecto-calreticulin (CALR) was detected by immunofluorescence staining. After 30 min incubation at 4 °C with primary CALR-specific antibody diluted 1/100 in 1% BSA in PBS, cells were washed and further incubated with 1/500 anti-rabbit secondary antibody for

30 min at 4 °C. After last washing steps, cells were stained with 1 µg/mL DAPI and analyzed via MACSQuant flow cytometer (Miltenyi Biotec, Bergisch Gladbach, Germany) and the percentage of $CALR^+$ cells among $DAPI^-$ cells was calculated.

Measurement of MX1 pathway activation

The assay followed the protocol developed by our group in the past [22]. Briefly, U2OS cells were seeded in 96-well plate and let adhere overnight. On the next day, cells were treated for 6 h and medium was refreshed for additional 24 h. HT29 MX1-GFP cells plated 2 days before were treated with supernatants transferred from U2OS, as well as with IFNα1 as an additional control, for 48 h. After fixation and automated microscopy described above, the percentage of $MX1^+$ cells was calculated based on the cellular GFP intensity, by applying an automated threshold optimally separating the negative and positive controls distributions.

Histone photoactivation and live cell spinning disk microscopy

U2OS cells expressing photoactivatable PAGFP-H2A [77] were used for histone eviction assessment, they were plated in 18 well glass bottom µ-Slides (81817, Ibidi) and let adhere. After overnight incubation, cells were imaged on a Nikon Ti2 Eclipse (Nikon France SAS, Champigny sur Marne, France) inverted microscope equipped with a W1 Spinning Disk 50 µm pinhole disk (Yokogawa, Japan), an incubator for temperature and CO_2 control (Okolab, Italy), a 60× NA 1.40 oil objective WD 0.130, a sCMOS PRIME 95B camera (Photometrics, AZ, USA), and a dual-output laser launch, which included 405, 488, 561, and 642 nm 30 mW lasers. The emission filter characteristics are as follows: 452/45 nm (Semrock Part# FF01-452/45); 470/24 nm (Chroma 348716); 525/50 nm (Semrock Part# FF03-525/50); 545/40 nm (Chroma 346986); (Semrock Part# FF01-609/54); and 708/75 nm (Semrock Part# FF01 708/75). The microscope was steered by Metamorph 7 software (MDS Analytical Technologies, Sunnyvale, CA, USA).

Contours of the partial region of the nucleus to be photoactivated were manually drawn using the MetaMorph software (Molecular Devices) on multiple cells in the same culture. Cells were treated with respective drugs and photoactivation was performed using 405 nm laser light. Photoactivated GFP-H2A was subsequently monitored over time with a multi-position time-lapse module every 5 min for a total duration of 1 h. Upon acquisition, micrographs were segmented using an iterative process. First, nuclei and photoactivated (PA) regions masks were generated at the initial timepoint, using the methods described above. Then, the non-linear transform between the nucleus image at time t_{-1} and t was gradually computed by means of registration (using R *RNiftyReg* package), and applied to the masks generated at t_{-1} to produce the masks at t. This procedure allowed to predict photoactivated regions, even when the intensity of their signal drastically decreased, and permitted to track nuclei over time. In a final step, timewise masks were used to evaluate the average GFP intensity of tracked nuclei in PA regions over time.

Immunoblotting

Cells were harvested, washed and lysed on ice with RIPA buffer supplemented with protease and phosphatase inhibitors. Samples were centrifuged at 12,000 g for 15 min at 4 °C and protein content was quantified using the BCA protein assay kit, adding bovine serum albumin (BSA) as standard. Subsequently, 20 µg of protein were dissolved in LDS sample buffer 4X and sample reducing agent 10X, then denaturated at 100 °C for 10 min. Protein samples were separated on pre-cast 4–12% polyacrylamide Bis-Tris gels in MOPS SDS Running buffer and electro-transferred to EtOH-activated PVDF membranes in transfer buffer (25 mM Tris, 190 mM glycine, 20% ethanol in H2O). Membranes were blocked in Tris-buffered saline with Tween®20 detergent (TBST, 20 mM Tris, pH7.5, 150 mM NaCL, 0.1% Tween®20 in H_2O) supplemented with 5% BSA for 1 h to prevent non-specific binding. Membranes were then probed with primary antibody against phospho-histone H2A.X (Ser139) antibody, diluted 1/1,000 in 5% BSA in TBST overnight at 4 °C on a rocking shaker. Equal loading was verified by means of β-actin diluted 1/10,000 in 5% BSA in TBST. The following day, membranes were extensively washed with TBST and incubated with goat anti-rabbit IgG (H+L) horseradish peroxidase (HRP)-labeled secondary antibody diluted 1/5,000 in 5% BSA in TBST for 1 h at room temperature. Immunostained proteins were visualized using the ECL™ Prime western blotting detection reagents and chemiluminescence images were acquired with an Amersham ImageQuant 800 Western blot imaging system (Cytiva, Marlborough, US). The densitometry quantification was performed using ImageJ software.

In vivo experimentation

Female wild-type C57Bl/6 mice (6–8 weeks old) were obtained from Envigo (Gannat, France). The animal facility of Gustave Roussy Cancer Campus housed the mice in a pathogen-free, temperature-controlled environment, where mice were kept in 12-hour light/dark cycles with unrestricted access to food and water. Animal experiments followed the EU Directive 63/2010 and were conducted under the protocol no. 2023120514306594, approved by the Ethical Committee of Gustave Roussy Cancer Campus (CEEA IRCIV/IGR no. 26, registered at the French Ministry of Research). Palpable tumors were

measured 2 to 3 days per week using a standard caliper as a surface calculated as longest dimension × perpendicular dimension × pi/4. Mice with tumors smaller than 25 mm^2 were considered as tumor free. Sacrifice was applied once tumors reached a maximum volume of 1,700 mm^2 or show any signs of discomfort.

Anticancer vaccination

MCA205 cells were seeded in T-175 flasks and, after overnight adhesion, treated with a selection of chemical agents to reach around 60% mortality after 24 h. After cell harvesting and washing, 10^6 cells were resuspended in 100 µL PBS and subcutaneously (*s.c.*) injected into the left flank of immunocompetent C57Bl/6 mice. Ten days later, mice were rechallenged with 10^5 living MCA205 cells *s.c.* injected into the contralateral flank of the mice, and tumor growth was monitored for the forthcoming weeks. Tumor-free mice were rechallenged with *s.c.* injection of 10^5 living MCA205 cells in the left flank of the mice, and $2x10^5$ living B16-F10 cells in the contralateral flank. Tumor growth was monitored until endpoint.

Tumor treatment

Tumor treatment experiment followed an established fibrosarcoma model. C57Bl/6 mice were *s.c.* inoculated in one flank with $5x10^5$ wild-type MCA205 cells. When tumors became palpable, mice were randomized into different groups with $n=8$ mice per group and 50 mg/kg BMH21 (diluted in physiological saline containing 10% PEG400, 10% Tween-80 and 4% DMSO), or the diluent alone was intraperitoneally (*i.p.*) injected. Two, 4 and 7 days later the treatment was repeated. For T cell depletion, mice received *i.p.* injections of 100 µg anti-CD4 plus 100 µg anti-CD8 specific depleting antibodies or 200 µg isotype diluted in PBS, the same day and 1, 5, 8 and 14 days after the pharmacological treatment. Tumor growth was monitored for the forthcoming weeks.

Ultrasound assessment of cardiac function

12-week-old C57BL/6JRj female mice were purchased from Janvier Labs. These experiments were approved by the responsible national agencies (Bundesministerium für Wissenschaft, Forschung und Wirtschaft, BMWFW, Austria: BMWFW-2020-0.824.559 and BMWFW-2024-0.697.697). Following a week of acclimatization, mice were randomized (1:1:1) to receive either vehicle (control), aclarubicin or BMH21. Aclarubicin-treated mice received 5 mg/kg *i.p.* injection once a week for 4 weeks (cumulative dose of 20 mg/kg). BMH21 was also administered *i.p.* at a dose of 50 mg/kg every two days for 4 times (cumulative dose of 200 mg/kg), similar to the protocol used for tumor treatment experiments. Later on, this group received weekly saline injections. After 4 weeks following the first injection, all mice were assessed using non-invasive echocardiography (Vevo3100, Fujifilm VisualSonics Inc., Canada) [84]. Briefly, mice were lightly anesthetized (5% for induction; 1.5% isoflurane for maintenance) and body temperature was kept at 37 °C using a temperature-controlled heating platform. Mice were placed in a supine position with their limbs in direct contact with non-invasive electrocardiogram leads for heart rate assessment. Pre-warmed ultrasound transmission gel was spread on a shaved chest to obtain cardiac tracings in the parasternal long axis using high-resolution 55 MHz linear-array probe. M-mode tracings were used to evaluate cardiac walls thickness and internal left ventricular dimensions at the level of the papillary muscles during systole and diastole. Ventricular volumes and myocardial mass were estimated using Teichholtz and Troy formulas, respectively. Ejection fraction and cardiac output were determined to assess systolic function, while left ventricular mass, left ventricular remodelling index and left ventricular end-diastolic volume were used to assess hypertrophy and dilation, respectively. Furthermore, a speckle-tracking software (Vevo Strain, Fujifilm VisualSonics Inc., Canada) was used for global longitudinal strain assessment. Generally, at least 3 stable cardiac cycles were averaged to obtain the reported parameters. Statistical significance was derived using ANOVA with Bonferroni post-hoc or Welch's test with Dunnett's T3 post-hoc test, as appropriate.

Quantitative structure-activity relationship (QSAR) modeling for nucleolar condensation prediction

In total, nine compound libraries of various sizes (listed in the "Chemical libraries and drugs" section) were screened for their ability to induce the condensation of nucleoli (CON) phenotype, as described in previous paragraphs. Each drug was then attributed a label: 0 when it induced an average CON probability < 0.4 (CON^-), 1 otherwise (CON^+). In the meantime, molecule SMILES were retrieved from the library providers, parsed and preprocessed by regenerating 2D coordinates and removing binding salts, to finally compute a set of 287 molecular descriptors. All these mentioned steps were performed using the R *rcdk* package. The obtained raw dataset was curated as follows: first, features with low variance (i.e., MAD = 0) and/or containing too many missing values (> 50%) were removed; in a second step, duplicate compounds were detected by computing the Tanimoto similiarity matrix from atom pairs and identifying similarities > 0.99, to be discarded. The curated dataset was finally split into training (8 libraries, $n=2{,}968$, 3.77% of which classified as CON^+) and validation datasets (NCI mechanistic set, $n=654$, 4.59% of CON^+) (Supplementary Material 3).

The training set was normalized by applying feature-wise min-max normalization, the missing values being

replaced by the median of the corresponding descriptor. Min, max, and median values were saved for applying the same transformations to any future data set.

This normalized training features set was thereafter used as a basis for defining the applicability domain (AD) of developed QSAR models; first, the overall feature's centroid was calculated, which next allowed to calculate for each individual compound its Euclidian distance d_{AD}. The distribution of these distances (notably the 95th and 99th quantiles) within the training set allowed us to define a confidence interval, which was thereafter referred as the AD.

Three model architectures were then defined for training, namely (i) deep neural network (NN), (ii) random forest (RF), (iii) xgboost (XG). Of note, the NN was constructed as a sequential model (each layer has single input and output tensors), containing 3 dense layers, totalizing 9,601 trainable parameters (Fig. S11a). It was compiled using AUC (Area Under the Curve) as accuracy metric, and BinaryCrossEntropy (BCE) as loss function, while the learning rate (LR) was set to 10^{-4} and the number of epochs to 125 for training tasks. Overfitting risk was limited by adding dropouts between each layer of the connected model. The XG model was set to use binary logistic regression, with LR = 0.3 and 50 epochs. The RF hyperparameters, i.e. the number of trees and feature subset size, were automatically optimized using the R *caret* package. As the training set was majorly imbalanced, classes were attributed weights inversely proportionally to their occurrence for all three models during the training process. For Monte Carlo cross-validation (MCCV) procedure, a total of 10 random splits were generated, each of them removing 20% of the original data set individuals (used as a testing set), with conserved ratios of classes. The 3 model architectures were then trained on each of the 10 instances, and their performance was evaluated by predicting the propensity of the compounds included in the NCI-mechanistic set to induce CON. As a primary evaluation metrics, the AUC was computed for each of the 30 trained QSAR models, and median as well as Median Absolute Deviation (MAD) were calculated by model type. This step permitted to define the most suitable QSAR model's type, by taking in consideration both performance and stability. In addition, model outputs were binarized by using a cutoff defined as the probability maximizing the F1-score, allowing to compute several discrete performance metrics such as Mathews Correlation Coefficient (MCC) or Binary Accuracy (BA). AUC, MCC and BA were summed up to compute a "performance score" enabling the selection of one of the 10 trained models from the previously kept model's type.

In a final validation step, a Y-scrambling procedure was performed to the best model type to ensure its specificity in predicting the CON phenotype. To achieve this goal, a hundred "scrambles" (i.e., the random permutation of individual labels in the original training set) was generated, each of it consisting in a training/testing pair (80, 20% of total individuals, respectively). After models' training, their performance was assessed using randomly generated testing sets, by evaluating AUC and loss. These values were then compared to those reported during the original MCCV procedure.

The QSAR Model was interpreted using the Local Interpretable Model-Agnostic Explanations (LIME) method, as described [85]. This procedure was set to highlight the two main molecular features contributing to the prediction of each single compound's CON phenotype from the previously-described validation set. These feature occurrences were summed up and expressed as a fraction of the total number of individuals in the data set, thus creating a "contributing weight" ranging from 0 (poor contributor) to 1 (highest contributor).

Retrospective in silico analysis of DTP NCI chemical data

SMILES from the DTP NCI chemical collection were retrieved from the NIH database at the following link: https://wiki.nci.nih.gov/display/NCIDTPdata/Chemical+Data. These records (n = 319 918) were parsed and pre-processed as described in the previous section and then filtered by removing compounds with a molecular weight > 1,500 Daltons (the main parameter highlighting outliers as defined by AD of the QSAR model). Molecular descriptors were then calculated for each of the 319,481 remaining molecules and treated as described above. This feature set was thereafter fed to the previously trained NN-based QSAR model to attribute a CON-inducing probability (p_{CON}) to each compound. The next step consisted in retrieving all available Medical Subject Headings (MeSH) terms associated with the chemical data set, using the PubMed PUG REST API (https://pubchem.ncbi.nlm.nih.gov/rest/pug). When omitting compounds already included in the training set utilized in previous sections, 10,948 compounds were associated with MeSH records. To detect any major drift in distributions between this subset and the original set, a Kolmogorov-Smirnov test was performed, and the D-value (the max difference between the two cumulative distributions) was extracted.

An enrichment analysis was performed on the 10,948 MeSH records, after splitting them into 2 categories ($p_{CON} \geq 0.98$, n = 167 and $p_{CON} < 0.98$, n = 10,777). Briefly, for each of the 449 unique MeSH terms (filtered by removing terms such as "Supplementary records" or "Chemicals and Drug Category"), occurrence was calculated in each group, expressed as its number of repetitions to the number of compounds present in the group. Two metrics were finally derived from this calculation: (i)

the ratio of occurrences between the two groups and (ii) the p-value resulting from γ^2 statistical test. The full dataset is freely available and can be downloaded at https://github.com/kroemerlab/NucleolAI/tree/main/RESOURCES/NIH_320K.

Statistical analysis

For high-throughput imaging experiments, unless otherwise specified, computed cell features were averaged by image. Most conditions being repeated in quadruplicate wells, with 4 viewfields per well, this resulted into 16 data points that were statistically reduced by computing median and median absolute deviation (MAD). Significance was evaluated by performing non-parametric pairwise Mann-Whitney tests against adequate controls. Low-throughput imaging experiments (photoactivation, holotomography) followed the same data-reduction procedure applied directly to cell data.

Data reduction procedures were also applied for producing the heatmap shown in Fig. 6e. First, the areas under the curves (AUC) of vaccination kinetics (described in the next paragraph) were calculated and their fold change to PBS control was computed. Vaccination efficacy was thereafter expressed by subtracting the resulting value to 1. Other variables from in *vitro* experiments were aggregated for each drug by reporting the 3rd quartile of the set of values from all concentrations. All statistical treatments described above were performed using freely available R software (http://www.r-project.org).

For in vivo vaccination and tumor treatment experiments, the required number of mice per group to achieve statistical significance was calculated using the "BiostaTGV" software based on expected results. Tumor growth data are depicted as dot plots or means ± SEM of mice belonging to the same group. Statistical significance was calculated using type II ANOVA test using the TumGrowth software package developed by our group [86], freely available at https://www.github.com/kroemerlab. Analysis of survival was performed using the Log-rank test with GraphPad Prism software 9 (San Diego, California, USA).

Abbreviations

ACLA	Aclarubicin
AD	Applicability domain
AI	Artificial intelligence
ATP	Adenosine triphosphate
AUC	Area under the curve
BA	Binary accuracy
BISA	Bisantrene
CALR	Calreticulin
CDDP	Cisplatin
CDK	Chemistry development kit
CNN	Convolutional neural network
CON	Condensation of nucleoli
CTR	Control
DACT	Dactinomycin
DAMPs	Danger-associated molecular patterns
DCNN	Deep convolutional neural network
DMSO	Dimethyl sulfoxide
DOXO	Doxorubicin
dsDNA	Double-stranded DNA
eIF2α	Eukaryotic initiation factor 2α
ER	Endoplasmic reticulum
ETO	Etoposide
EU	5-ethynyl uridine
FBL	Fibrillarin
FC	Fold change
GANs	Generative adversarial networks
Grad-CAM	Gradient-weighted class activation mapping
HMGB1	High-mobility group B1
ICD	Immunogenic cell death
IFN	Interferon
LIME	Local interpretable model-agnostic explanations
LR	Learning rate
MAD	Median absolute deviation
MCC	Matthews correlation coefficient
MCCV	Monte Carlo cross-validation
MTX	Mitoxantrone
NCL	Nucleolin
NN	Neural network
OXA	Oxaliplatin
PeIF2α	Phosphorylation of eukaryotic initiation factor 2α
PLICA	Plicamycin
PR	Photoactivated region
PRRs	Pattern recognition receptors
QSAR	Quantitative structure activity relationship
RF	Random forest
ROI	Region of interest
SD	Standard deviation
SEM	Standard error of the mean
Sik-SP	Sik-similar protein
THAPS	Thapsigargin
TL	Transmitted light
WT	Wild-type
XG	Xgboost

Supplementary Information

The online version contains supplementary material available at https://doi.org/10.1186/s12943-024-02189-3.

Supplementary Material 1: Random forest classifier variables importance. This table gives the correspondence between variable rank (as shown in Fig. 1c) and its name ("feature_name"), as well as its corresponding Gini index mean ("importance"). The "Surf" prefix indicates the quantification of total area from the segmented compartment (in pixels), as reported in Supplemental Material 3. The nomenclature of the other parameters can be retrieved using references (81, 82).

Supplementary Material 2: Training set used for refining the CNN classifier. The numbers of patches for each case are reported. Each line of the table indicates: the compound used ("Treatment"), its PubChem ID, the duration of the treatment ("Duration"), the class it corresponds to (0: control; 1:CON$^+$, 2:dead), and the cell line that was treated.

Supplementary Material 3: QSAR model training set. This table contains three columns: (i) "Molecule Name", the molecule identifier. (ii) "SMILES", the molecule SMILES annotation. (iii) "CON", which equals (1) if the molecule is considered as a CON inducer, else (0).(iv) "Library", which indicate the source library of the molecule. (v) "Set", which defines if the molecule was used for training or validating the model.

Supplementary Material 4: Definition of the descriptors of the Chemistry Development Kit (CDK). This table recapitulates the definitions of the different parameters computed, retrieved from https://cdk.github.io/ and https://docs.ochem.eu/x/GgJr.html.

Supplementary Material 5: Precise imaging parameters used in microscopy experiments. These tables report fluorophore/antibody references, as well as their spectral properties and the microscopy filter sets/objectives used

for imaging them. The "Cell painting" table also indicates the concrete values of the "top hat" kernel size, as well as the center z of sigmoid transform, as described in the "Image processing procedures" section.

Supplementary Material 6: Annotated results from the DNA/RNA synthesis library screening. This table displays the values presented in Fig. 4b/S3a. Additional columns show molecule synonyms and SMILES annotations (retrieved from the PubChem database), as well as the selected concentrations for the displayed effects.

Supplementary Material 7: Supplementary figures and legends.

Acknowledgements
The authors thank Pierre-Alexandre Vidi for providing the U2OS PAGFP-H2A cell line, Tudor Manoliu of the Gustave Roussy Microscopy Core Facility for his help with the photoactivation experiments, Donal Naylor for his review of the manuscript, the National Cancer Institute (NCI) for the generous supply of drugs and Nanolive for providing access to their instrument. GK is supported by the Ligue contre le Cancer (équipe labellisée); Agence Nationale de la Recherche (ANR-22-CE14-0066 VIVORUSH, ANR-23-CE44-0030 COPPERMAC, ANR-23-R4HC-0006 Ener-LIGHT); Association pour la recherche sur le cancer (ARC); Cancéropôle Ile-de-France; Fondation pour la Recherche Médicale (FRM); a donation by Elior; European Joint Programme on Rare Diseases (EJPRD) Wilsonmed; European Research Council Advanced Investigator Award (ERC-2021-ADG, Grant No. 101052444; project acronym: ICD-Cancer, project title: Immunogenic cell death (ICD) in the cancer-immune dialogue); The ERA4 Health CardInnov Grant Ener-LIGHT; European Union Horizon 2020 research and innovation programmes Oncobiome (grant agreement number: 825410, Project Acronym: ONCOBIOME, Project title: Gut OncoMicrobiome Signatures [GOMS] associated with cancer incidence, prognosis and prediction of treatment response, Prevalung (grant agreement number 101095604, Project Acronym: PREVALUNG EU, project title: Biomarkers affecting the transition from cardiovascular disease to lung cancer: towards stratified interception), Neutrocure (grant agreement number 861878: Project Acronym: Neutrocure; project title: Development of "smart" amplifiers of reactive oxygen species specific to aberrant polymorphonuclear neutrophils for treatment of inflammatory and autoimmune diseases, cancer and myeloablation); National support managed by the Agence Nationale de la Recherche under the France 2030 programme (reference number 21-ESRE-0028, ESR/Equipex+ Onco-Pheno-Screen); Hevolution Network on Senescence in Aging (reference HF-E Einstein Network); Institut National du Cancer (INCa); Institut Universitaire de France; LabEx Immuno-Oncology ANR-18-IDEX-0001; a Cancer Research ASPIRE Award from the Mark Foundation; PAIR-Obésité INCa_1873, the RHUs Immunolife and LUCA-pi (ANR-21-RHUS-0017 and ANR-23-RHUS-0010, both dedicated to France Relance 2030); Seerave Foundation; SIRIC Cancer Research and Personalized Medicine (CARPEM, SIRIC CARPEM INCa-DGOS-Inserm-ITMO Cancer_18006 supported by Institut National du Cancer, Ministère des Solidarités et de la Santé and INSERM). This study contributes to the IdEx Université de Paris Cité ANR-18-IDEX-0001.

Author contributions
GC performed experimental procedures. AS performed bioinformatic analysis. LP and ZL conducted in vivo vaccination and tumor treatment. JH contributed to assessment of transcription inhibition to correlate various in vitro methods. AP contributed to the in vitro assessment of ICD hallmarks. STS and MA conducted cardiotoxicity study. GC and AS generated figures. GK, AS and GC conceived and directed the project, and wrote the manuscript. All authors have read and agreed to the published version of the manuscript.

Funding
GK is supported by the Ligue contre le Cancer (équipe labellisée); Agence Nationale de la Recherche (ANR-22-CE14-0066 VIVORUSH, ANR-23-CE44-0030 COPPERMAC, ANR-23-R4HC-0006 Ener-LIGHT); Association pour la recherche sur le cancer (ARC); Cancéropôle Ile-de-France; Fondation pour la Recherche Médicale (FRM); a donation by Elior; European Joint Programme on Rare Diseases (EJPRD) Wilsonmed; European Research Council Advanced Investigator Award (ERC-2021-ADG, Grant No. 101052444; project acronym: ICD-Cancer, project title: Immunogenic cell death (ICD) in the cancer-immune dialogue); The ERA4 Health CardInnov Grant Ener-LIGHT; European Union Horizon 2020 research and innovation programmes Oncobiome (grant agreement number: 825410, Project Acronym: ONCOBIOME, Project title: Gut OncoMicrobiome Signatures [GOMS] associated with cancer incidence, prognosis and prediction of treatment response, Prevalung (grant agreement number 101095604, Project Acronym: PREVALUNG EU, project title: Biomarkers affecting the transition from cardiovascular disease to lung cancer: towards stratified interception), Neutrocure (grant agreement number 861878: Project Acronym: Neutrocure; project title: Development of "smart" amplifiers of reactive oxygen species specific to aberrant polymorphonuclear neutrophils for treatment of inflammatory and autoimmune diseases, cancer and myeloablation); National support managed by the Agence Nationale de la Recherche under the France 2030 programme (reference number 21-ESRE-0028, ESR/Equipex + Onco-Pheno-Screen); Hevolution Network on Senescence in Aging (reference HF-E Einstein Network); Institut National du Cancer (INCa); Institut Universitaire de France; LabEx Immuno-Oncology ANR-18-IDEX-0001; a Cancer Research ASPIRE Award from the Mark Foundation; PAIR-Obésité INCa_1873, the RHUs Immunolife and LUCA-pi (ANR-21-RHUS-0017 and ANR-23-RHUS-0010, both dedicated to France Relance 2030); Seerave Foundation; SIRIC Cancer Research and Personalized Medicine (CARPEM, SIRIC CARPEM INCa-DGOS-Inserm-ITMO Cancer_18006 supported by Institut National du Cancer, Ministère des Solidarités et de la Santé and INSERM). This study contributes to the IdEx Université de Paris Cité ANR-18-IDEX-0001.

Data availability
All retrieved and computed compound information (descriptors, CON probability) were uploaded on a public open-access repository (https://github.com/kroemerlab/NucleolAI/tree/main/RESOURCES/NIH_320K). Other data is provided within the manuscript or supplementary information files.

Declarations

Ethical approval
Animal experiments followed the EU Directive 63/2010 and were conducted under the protocol no. 2023120514306594, approved by the Ethical Committee of Gustave Roussy Cancer Campus (CEEA IRCIV/IGR no. 26, registered at the French Ministry of Research) and by the national agency Bundesministerium für Wissenschaft, Forschung und Wirtschaft, BMWFW, Austria under the protocols no. BMWFW-2020-0.824.559 and BMWFW-2024-0.697.697).

Consent for publication
Not applicable.

Competing interests
GK has been holding research contracts with Daiichi Sankyo, Eleor, Kaleido, Lytix Pharma, PharmaMar, Osasuna Therapeutics, Samsara Therapeutics, Sanofi, Sutro, Tollys, and Vascage. GK is on the Board of Directors of the Bristol Myers Squibb Foundation France. GK is a scientific co-founder of everImmune, Osasuna Therapeutics, Samsara Therapeutics and Therafast Bio. GK is in the scientific advisory boards of Hevolution, Institut Servier, Longevity Vision Funds and Rejuveron Life Sciences. GK is the inventor of patents covering therapeutic targeting of aging, cancer, cystic fibrosis and metabolic disorders. GK's wife, Laurence Zitvogel, has held research contracts with Glaxo Smyth Kline, Incyte, Lytix, Kaleido, Innovate Pharma, Daiichi Sankyo, Pilege, Merus, Transgene, 9 m, Tusk and Roche, was on the on the Board of Directors of Transgene, is a cofounder of everImmune, and holds patents covering the treatment of cancer and the therapeutic manipulation of the microbiota. GK's brother, Romano Kroemer, was an employee of Sanofi and now consults for Boehringer-Ingelheim. The funders had no role in the design of the study; in the writing of the manuscript, or in the decision to publish the results. No disclosures were reported by the other authors.

Author details
[1]Centre de Recherche des Cordeliers, Equipe Labellisée par la Ligue Contre le Cancer, Université de Paris, Institut Universitaire de France, Sorbonne Université, Inserm U1138, Paris, France
[2]Onco-Pheno-Screen Platform, Centre de Recherche des Cordeliers, Paris, France
[3]Metabolomics and Cell Biology Platforms, Institut Gustave Roussy, Villejuif, France
[4]International Centre for T1D, Pediatric Clinical Research Center Romeo ed Enrica Invernizzi, Department of Biomedical and Clinical Sciences, Università Degli Studi di Milano, Milan, Italy

[5]Centre de Recherche en Cancérologie de Lyon (CRCL), Equipe Oncopharmacologie, Faculté Rockfeller, Lyon, France
[6]Department of Cardiology, Medical University of Graz, Graz, Austria
[7]BioTechMed Graz, Graz, Austria
[8]Department of Biology, Institut du Cancer Paris CARPEM, Hôpital Européen Georges Pompidou, AP-HP, Paris, France
[9]Centre de Recherche des Cordeliers, 15 Rue de l'École de Médecine, Paris 75006, France

Received: 4 October 2024 / Accepted: 28 November 2024
Published online: 20 December 2024

References

1. Kroemer G, Galassi C, Zitvogel L, Galluzzi L. Immunogenic cell stress and death. Nat Immunol. 2022;23(4):487–500.
2. Clucas J, Meier P. Roles of RIPK1 as a stress sentinel coordinating cell survival and immunogenic cell death. Nat Rev Mol Cell Biol. 2023;24(11):835–52.
3. Catanzaro E, Demuynck R, Naessens F, Galluzzi L, Krysko DV. Immunogenicity of ferroptosis in cancer: a matter of context? Trends Cancer. 2024;10(5):407–16.
4. Galluzzi L, Guilbaud E, Schmidt D, Kroemer G, Marincola FM. Targeting immunogenic cell stress and death for cancer therapy. Nat Rev Drug Discov. 2024;23(6):445–60.
5. Pfirschke C, Engblom C, Rickelt S, Cortez-Retamozo V, Garris C, Pucci F, et al. Immunogenic chemotherapy sensitizes tumors to checkpoint blockade therapy. Immunity. 2016;44(2):343–54.
6. Thibaudin M, Fumet JD, Chibaudel B, Bennouna J, Borg C, Martin-Babau J, et al. First-line durvalumab and tremelimumab with chemotherapy in RAS-mutated metastatic colorectal cancer: a phase 1b/2 trial. Nat Med. 2023;29(8):2087–98.
7. Shitara K, Van Cutsem E, Bang YJ, Fuchs C, Wyrwicz L, Lee KW, et al. Efficacy and safety of Pembrolizumab or Pembrolizumab Plus Chemotherapy vs Chemotherapy alone for patients with First-line, Advanced Gastric Cancer: the KEYNOTE-062 phase 3 Randomized Clinical Trial. JAMA Oncol. 2020;6(10):1571–80.
8. Janjigian YY, Shitara K, Moehler M, Garrido M, Salman P, Shen L, et al. First-line nivolumab plus chemotherapy versus chemotherapy alone for advanced gastric, gastro-oesophageal junction, and oesophageal adenocarcinoma (CheckMate 649): a randomised, open-label, phase 3 trial. Lancet. 2021;398(10294):27–40.
9. Liu P, Chen J, Zhao L, Hollebecque A, Kepp O, Zitvogel L, et al. PD-1 blockade synergizes with oxaliplatin-based, but not cisplatin-based, chemotherapy of gastric cancer. Oncoimmunology. 2022;11(1):2093518.
10. Voorwerk L, Slagter M, Horlings HM, Sikorska K, van de Vijver KK, de Maaker M, et al. Immune induction strategies in metastatic triple-negative breast cancer to enhance the sensitivity to PD-1 blockade: the TONIC trial. Nat Med. 2019;25(6):920–8.
11. Rossevold AH, Andresen NK, Bjerre CA, Gilje B, Jakobsen EH, Raj SX, et al. Atezolizumab plus anthracycline-based chemotherapy in metastatic triple-negative breast cancer: the randomized, double-blind phase 2b ALICE trial. Nat Med. 2022;28(12):2573–83.
12. Jiang Z, Ouyang Q, Sun T, Zhang Q, Teng Y, Cui J, et al. Toripalimab plus nab-paclitaxel in metastatic or recurrent triple-negative breast cancer: a randomized phase 3 trial. Nat Med. 2024;30(1):249–56.
13. Gao J, Xiong A, Liu J, Li X, Wang J, Zhang L et al. PANoptosis: bridging apoptosis, pyroptosis, and necroptosis in cancer progression and treatment. Cancer Gene Ther. 2024;31(7):970–83.
14. Obeid M, Tesniere A, Ghiringhelli F, Fimia GM, Apetoh L, Perfettini JL, et al. Calreticulin exposure dictates the immunogenicity of cancer cell death. Nat Med. 2007;13(1):54–61.
15. Michaud M, Martins I, Sukkurwala AQ, Adjemian S, Ma Y, Pellegatti P, et al. Autophagy-dependent anticancer immune responses induced by chemotherapeutic agents in mice. Science. 2011;334(6062):1573–7.
16. Sistigu A, Yamazaki T, Vacchelli E, Chaba K, Enot DP, Adam J, et al. Cancer cell-autonomous contribution of type I interferon signaling to the efficacy of chemotherapy. Nat Med. 2014;20(11):1301–9.
17. Apetoh L, Ghiringhelli F, Tesniere A, Obeid M, Ortiz C, Criollo A, et al. Toll-like receptor 4-dependent contribution of the immune system to anticancer chemotherapy and radiotherapy. Nat Med. 2007;13(9):1050–9.
18. Vacchelli E, Ma Y, Baracco EE, Sistigu A, Enot DP, Pietrocola F, et al. Chemotherapy-induced antitumor immunity requires formyl peptide receptor 1. Science. 2015;350(6263):972–8.
19. Galluzzi L, Humeau J, Buque A, Zitvogel L, Kroemer G. Immunostimulation with chemotherapy in the era of immune checkpoint inhibitors. Nat Rev Clin Oncol. 2020;17(12):725–41.
20. Menger L, Vacchelli E, Adjemian S, Martins I, Ma Y, Shen S, et al. Cardiac glycosides exert anticancer effects by inducing immunogenic cell death. Sci Transl Med. 2012;4(143):143ra99.
21. Galluzzi L, Vitale I, Warren S, Adjemian S, Agostinis P, Martinez AB et al. Consensus guidelines for the definition, detection and interpretation of immunogenic cell death. J Immunother Cancer. 2020;8(1).
22. Zhou H, Forveille S, Sauvat A, Yamazaki T, Senovilla L, Ma Y, et al. The oncolytic peptide LTX-315 triggers immunogenic cell death. Cell Death Dis. 2016;7(3):e2134.
23. Xie W, Forveille S, Iribarren K, Sauvat A, Senovilla L, Wang Y, et al. Lurbinectedin synergizes with immune checkpoint blockade to generate anticancer immunity. Oncoimmunology. 2019;8(11):e1656502.
24. Montes de Oca R, Alavi AS, Vitali N, Bhattacharya S, Blackwell C, Patel K, et al. Belantamab Mafodotin (GSK2857916) drives immunogenic cell death and Immune-mediated antitumor responses in vivo. Mol Cancer Ther. 2021;20(10):1941–55.
25. Nielsen M, Monberg T, Sundvold V, Albieri B, Hovgaard D, Petersen MM, et al. LTX-315 and adoptive cell therapy using tumor-infiltrating lymphocytes generate tumor specific T cells in patients with metastatic soft tissue sarcoma. Oncoimmunology. 2024;13(1):2290900.
26. Panaretakis T, Kepp O, Brockmeier U, Tesniere A, Bjorklund AC, Chapman DC, et al. Mechanisms of pre-apoptotic calreticulin exposure in immunogenic cell death. EMBO J. 2009;28(5):578–90.
27. Bezu L, Sauvat A, Humeau J, Gomes-da-Silva LC, Iribarren K, Forveille S, et al. eIF2alpha phosphorylation is pathognomonic for immunogenic cell death. Cell Death Differ. 2018;25(8):1375–93.
28. Fucikova J, Becht E, Iribarren K, Goc J, Remark R, Damotte D, et al. Calreticulin expression in human non-small cell lung cancers correlates with increased Accumulation of Antitumor Immune Cells and favorable prognosis. Cancer Res. 2016;76(7):1746–56.
29. Sauvat A, Cerrato G, Humeau J, Leduc M, Kepp O, Kroemer G. High-throughput label-free detection of DNA-to-RNA transcription inhibition using brightfield microscopy and deep neural networks. Comput Biol Med. 2021;133:104371.
30. Humeau J, Sauvat A, Cerrato G, Xie W, Loos F, Iannantuoni F, et al. Inhibition of transcription by dactinomycin reveals a new characteristic of immunogenic cell stress. EMBO Mol Med. 2020;12(5):e11622.
31. Bray MA, Singh S, Han H, Davis CT, Borgeson B, Hartland C, et al. Cell painting, a high-content image-based assay for morphological profiling using multiplexed fluorescent dyes. Nat Protoc. 2016;11(9):1757–74.
32. Kepp O, Senovilla L, Vitale I, Vacchelli E, Adjemian S, Agostinis P, et al. Consensus guidelines for the detection of immunogenic cell death. Oncoimmunology. 2014;3(9):e955691.
33. Nagao Y, Sakamoto M, Chinen T, Okada Y, Takao D. Robust classification of cell cycle phase and biological feature extraction by image-based deep learning. Mol Biol Cell. 2020;31(13):1346–54.
34. Selvaraju RR, Cogswell M, Das A, Vedantam R, Parikh D, Batra D. Grad-CAM: visual explanations from deep networks via gradient-based localization. Int J Comput Vision. 2020;128(2):336–59.
35. Casares N, Pequignot MO, Tesniere A, Ghiringhelli F, Roux S, Chaput N, et al. Caspase-dependent immunogenicity of doxorubicin-induced tumor cell death. J Exp Med. 2005;202(12):1691–701.
36. Jao CY, Salic A. Exploring RNA transcription and turnover in vivo by using click chemistry. Proc Natl Acad Sci U S A. 2008;105(41):15779–84.
37. Peltonen K, Colis L, Liu H, Trivedi R, Moubarek MS, Moore HM, et al. A targeting modality for destruction of RNA polymerase I that possesses anticancer activity. Cancer Cell. 2014;25(1):77–90.
38. Sauvat A, Leduc M, Muller K, Kepp O, Kroemer G. ColocalizR: an open-source application for cell-based high-throughput colocalization analysis. Comput Biol Med. 2019;107:227–34.
39. Yakimovich A, Witte R, Andriasyan V, Georgi F, Greber UF. Label-Free Digital Holo-Tomographic Microscopy reveals Virus-Induced Cytopathic effects in live cells. mSphere. 2018;3(6).
40. Barsanti L, Birindelli L, Sbrana F, Lombardi G, Gualtieri P. Advanced Microscopy Techniques for Molecular Biophysics. Int J Mol Sci. 2023;24(12).

41. Panaretakis T, Joza N, Modjtahedi N, Tesniere A, Vitale I, Durchschlag M, et al. The co-translocation of ERp57 and calreticulin determines the immunogenicity of cell death. Cell Death Differ. 2008;15(9):1499–509.
42. Qiao X, van der Zanden SY, Wander DPA, Borras DM, Song JY, Li X, et al. Uncoupling DNA damage from chromatin damage to detoxify doxorubicin. Proc Natl Acad Sci U S A. 2020;117(26):15182–92.
43. Tesniere A, Schlemmer F, Boige V, Kepp O, Martins I, Ghiringhelli F, et al. Immunogenic death of colon cancer cells treated with oxaliplatin. Oncogene. 2010;29(4):482–91.
44. Harding HP, Zhang Y, Ron D. Protein translation and folding are coupled by an endoplasmic-reticulum-resident kinase. Nature. 1999;397(6716):271–4.
45. Hossain DMS, Javaid S, Cai M, Zhang C, Sawant A, Hinton M, et al. Dinaciclib induces immunogenic cell death and enhances anti-PD1-mediated tumor suppression. J Clin Invest. 2018;128(2):644–54.
46. Hall MD, Telma KA, Chang KE, Lee TD, Madigan JP, Lloyd JR, et al. Say no to DMSO: dimethylsulfoxide inactivates cisplatin, carboplatin, and other platinum complexes. Cancer Res. 2014;74(14):3913–22.
47. Chang X, Bian M, Liu L, Yang J, Yang Z, Wang Z, et al. Induction of immunogenic cell death by novel platinum-based anticancer agents. Pharmacol Res. 2023;187:106556.
48. Galsky MD, Guan X, Rishipathak D, Rapaport AS, Shehata HM, Banchereau R, et al. Immunomodulatory effects and improved outcomes with cisplatin- versus carboplatin-based chemotherapy plus atezolizumab in urothelial cancer. Cell Rep Med. 2024;5(2):101393.
49. Bruno PM, Liu Y, Park GY, Murai J, Koch CE, Eisen TJ, et al. A subset of platinum-containing chemotherapeutic agents kills cells by inducing ribosome biogenesis stress. Nat Med. 2017;23(4):461–71.
50. Pang B, Qiao X, Janssen L, Velds A, Groothuis T, Kerkhoven R, et al. Drug-induced histone eviction from open chromatin contributes to the chemotherapeutic effects of doxorubicin. Nat Commun. 2013;4:1908.
51. Gujar S, Pol JG, Kumar V, Lizarralde-Guerrero M, Konda P, Kroemer G et al. Tutorial: design, production and testing of oncolytic viruses for cancer immunotherapy. Nat Protoc. 2024;19(9):2540–570
52. Tesniere A, Apetoh L, Ghiringhelli F, Joza N, Panaretakis T, Kepp O, et al. Immunogenic cancer cell death: a key-lock paradigm. Curr Opin Immunol. 2008;20(5):504–11.
53. Kepp O, Sauvat A, Leduc M, Forveille S, Liu P, Zhao L, et al. A fluorescent biosensor-based platform for the discovery of immunogenic cancer cell death inducers. Oncoimmunology. 2019;8(8):1606665.
54. Alzeibak R, Mishchenko TA, Shilyagina NY, Balalaeva IV, Vedunova MV, Krysko DV. Targeting immunogenic cancer cell death by photodynamic therapy: past, present and future. J Immunother Cancer. 2021;9(1).
55. Kyriakidis S, Stevely WS. The effect of herpesvirus infection on ribosomal RNA synthesis and on nucleolar size and number in HeLa cells. Arch Virol. 1982;71(1):79–83.
56. Dudley RE, Svoboda DJ, Klaassen CD. Time course of cadmium-induced ultrastructural changes in rat liver. Toxicol Appl Pharmacol. 1984;76(1):150–60.
57. Jenkins LW, Povlishock JT, Lewelt W, Miller JD, Becker DP. The role of postischemic recirculation in the development of ischemic neuronal injury following complete cerebral ischemia. Acta Neuropathol. 1981;55(3):205–20.
58. Nassiri MR, Gilloteaux J, Taichman RS, Drach JC. Ultrastructural aspects of cytomegalovirus-infected fibroblastic stromal cells of human bone marrow. Tissue Cell. 1998;30(4):398–406.
59. Ortiz R, Echeverria OM, Salgado R, Escobar ML, Vazquez-Nin GH. Fine structural and cytochemical analysis of the processes of cell death of oocytes in atretic follicles in new born and prepubertal rats. Apoptosis. 2006;11(1):25–37.
60. de Los Santos-Velazquez AI, de Oya IG, Manzano-Lopez J, Monje-Casas F. Late rDNA condensation ensures timely Cdc14 release and coordination of Mitotic Exit Signaling with Nucleolar Segregation. Curr Biol. 2017;27(21):3248–63. e5.
61. Clemente-Blanco A. Nucleolar condensation: a new mechanism to Control Mitotic exit. Curr Biol. 2017;27(22):R1220–2.
62. Crozet N. Effects of actinomycin D and cycloheximide on the nucleolar ultrastructure of porcine oocytes. Biol Cell. 1983;48(1):25–9.
63. Jitsukawa M, Kyogoku H, Ogushi S, Miyano T. Effects of proteasome inhibitors on the nucleolar size of porcine oocytes. J Reprod Dev. 2012;58(1):162–6.
64. Snyers L, Laffer S, Lohnert R, Weipoltshammer K, Schofer C. CX-5461 causes nucleolar compaction, alteration of peri- and intranucleolar chromatin arrangement, an increase in both heterochromatin and DNA damage response. Sci Rep. 2022;12(1):13972.
65. Dzidziguri DV, Chelidze PV, Zarandia MA, Cherkezia EC, Tumanishvili GD. Transcriptional activity and ultrastructure of morphologically different types of nucleoli isolated from hepatocytes of normal and hepatectomized rats. Epithel Cell Biol. 1994;3(2):54–60.
66. Nakamoto K, Ito A, Watabe K, Koma Y, Asada H, Yoshikawa K, et al. Increased expression of a nucleolar Nop5/Sik family member in metastatic melanoma cells: evidence for its role in nucleolar sizing and function. Am J Pathol. 2001;159(4):1363–74.
67. Riback JA, Zhu L, Ferrolino MC, Tolbert M, Mitrea DM, Sanders DW, et al. Composition-dependent thermodynamics of intracellular phase separation. Nature. 2020;581(7807):209–14.
68. Sharp PA, Chakraborty AK, Henninger JE, Young RA. RNA in formation and regulation of transcriptional condensates. RNA. 2022;28(1):52–7.
69. Mokin YI, Gavrilova AA, Fefilova AS, Kuznetsova IM, Turoverov KK, Uversky VN et al. Nucleolar- and nuclear-stress-Induced Membrane-less organelles: a Proteome Analysis through the prism of liquid-liquid phase separation. Int J Mol Sci. 2023;24(13).
70. Bokros M, Balukoff NC, Grunfeld A, Sebastiao M, Beurel E, Bourgault S, et al. RNA tailing machinery drives amyloidogenic phase transition. Proc Natl Acad Sci U S A. 2024;121(23):e2316734121.
71. Kim E, Kwon I. Phase transition of fibrillarin LC domain regulates localization and protein interaction of fibrillarin. Biochem J. 2021;478(4):799–810.
72. Mensah MA, Niskanen H, Magalhaes AP, Basu S, Kircher M, Sczakiel HL, et al. Aberrant phase separation and nucleolar dysfunction in rare genetic diseases. Nature. 2023;614(7948):564–71.
73. Deng J, Zhong YF, Wu YP, Luo Z, Sun YM, Wang GE, et al. Carnosine attenuates cyclophosphamide-induced bone marrow suppression by reducing oxidative DNA damage. Redox Biol. 2018;14:1–6.
74. Makarevich O, Sabirzhanov B, Aubrecht TG, Glaser EP, Polster BM, Henry RJ, et al. Mithramycin selectively attenuates DNA-damage-induced neuronal cell death. Cell Death Dis. 2020;11(7):587.
75. Bouwman P, Jonkers J. The effects of deregulated DNA damage signalling on cancer chemotherapy response and resistance. Nat Rev Cancer. 2012;12(9):587–98.
76. Goldstein M, Kastan MB. The DNA damage response: implications for tumor responses to radiation and chemotherapy. Annu Rev Med. 2015;66:129–43.
77. Locatelli M, Lawrimore J, Lin H, Sanaullah S, Seitz C, Segall D, et al. DNA damage reduces heterogeneity and coherence of chromatin motions. Proc Natl Acad Sci U S A. 2022;119(29):e2205166119.
78. Bezu L, Humeau J, Leduc M, Pan H, Kroemer G, Kepp O. Assessment of eIF2alpha phosphorylation during immunogenic cell death. Methods Cell Biol. 2022;172:83–98.
79. Cerrato G, Humeau J, Sauvat A, Kepp O, Kroemer G. Assessment of transcription inhibition as a characteristic of immunogenic cell death. Methods Cell Biol. 2022;172:67–82.
80. Sato A, Buque A, Yamazaki T, Bloy N, Petroni G, Galluzzi L. Immunofluorescence microscopy-based assessment of cytosolic DNA accumulation in mammalian cells. STAR Protoc. 2021;2(2):100488.
81. Pau G, Fuchs F, Sklyar O, Boutros M, Huber W. EBImage–an R package for image processing with applications to cellular phenotypes. Bioinformatics. 2010;26(7):979–81.
82. Haralick RM, Shanmugam K, Dinstein I. Textural features for image classification. IEEE Trans Syst Man Cybernetics. 1973;SMC–3(6):610–21.
83. Goodfellow IJ, Pouget-Abadie J, Mirza M, Xu B, Warde-Farley D, Ozair S et al. Generative Adversarial Networks. arXiv [statML]. 2014.
84. Abdellatif M, Trummer-Herbst V, Heberle AM, Humnig A, Pendl T, Durand S, et al. Fine-tuning Cardiac insulin-like Growth factor 1 receptor signaling to Promote Health and Longevity. Circulation. 2022;145(25):1853–66.
85. Ribeiro MT, Singh S, Guestrin C. Why should I trust you? Explaining the predictions of any classifier. arXiv [csLG]; 2016.
86. Enot DP, Vacchelli E, Jacquelot N, Zitvogel L, Kroemer G. TumGrowth: an open-access web tool for the statistical analysis of tumor growth curves. Oncoimmunology. 2018;7(9):e1462431.

Publisher's note